Bioactive Materials 45 (2025) 363–387

Contents lists available at ScienceDirect

Bioactive Materials

journal homepage: www.keaipublishing.com/en/journals/bioactive-materials

Reduction reactions dominate the interactions between Mg alloys and cells: Understanding the mechanisms

Jua Kim [a,b], Jeremy L. Gilbert [b,c], William W. Lv [d], Ping Du [a,**], Haobo Pan [a,e,f,*]

[a] Shenzhen Key Laboratory of Marine Biomaterials, CAS-HK Joint Lab of Biomaterials, Shenzhen Institute of Advanced Technology, Chinese Academy of Sciences, 1068 Xueyuan Avenue, Shenzhen University Town, Shenzhen, 518055, PR China
[b] Syracuse Biomaterials Institute, Syracuse University, 318 Bowne Hall, Syracuse University, Syracuse, NY, 13244, USA
[c] Clemson- Medical University of South Carolina Bioengineering Program, Department of Bioengineering, Clemson University, 68 Presidents St, Charleston, SC, 39425, USA
[d] Department of Orthopaedics and Traumatology, Li Ka Shing Faculty of Medicine, The University of Hong Kong, Hong Kong, 999077, PR China
[e] Shenzhen Healthemes Biotechnology Co. Ltd, Shenzhen, 518102, PR China
[f] College of Chemical Engineering, Xinjiang Normal University, Urumqi, 830054, PR China

ARTICLE INFO

Keywords:
Magnesium alloys
Electrochemical reactions
Mg ions
Alkaline pH
Reactive oxygen species

ABSTRACT

Magnesium (Mg) alloys are popular biodegradable metals studied for orthopedic and cardiovascular applications, mainly because Mg ions are essential trace elements known to promote angiogenesis and osteogenesis. However, Mg corrosion consists of oxidation and reduction reactions that produce by-products, such as hydrogen gas, reactive oxygen species, and hydroxides. It is still unclear how all these by-products and Mg ions concomitantly alter the microenvironment and cell behaviors spatially and temporally. This study shows that Mg corrosion can enhance cell proliferation by reducing intracellular ROS. However, Mg cannot decrease ROS and promote cell proliferation in simulated inflammatory conditions, meaning the microenvironment is critical. Furthermore, cells may respond to Mg ions differently in chronic or acute alkaline pH or oxidative stress. Depending on the corrosion rate, Mg modulates HIF1α and many signaling pathways like PI3K/AKT/mTOR, mitophagy, cell cycle, and oxidative phosphorylation. Therefore, this study provides a fundamental insight into the importance of reduction reactions in Mg alloys.

1. Introduction

Biomaterial research has advanced quickly in recent years, where our new generation of biomaterials are now termed “smart biomaterials” that can sense the microenvironment, release ions, chemicals, drugs, biomolecules, or other substances in response to external stimuli (e.g., pH, hypoxia, oxidative stress, etc.), and adapt to the changes over time [1]. However, despite our extensive efforts in improving our biomaterials, traditional metals like titanium (Ti), cobalt-chromium (CoCr), and stainless steel (SS) alloys remain most widely used for orthopedic, cardiovascular and dental applications, dominating the market of biomaterials globally estimated about 31.53 billion USD in 2021 [2]. Therefore, metal-based biomaterials, including permanent and biodegradable metals, will be the largest class of biomaterials used for hard tissues in the foreseeable future. However, metal corrosion and biological/biochemical/biomechanical interactions between metals and cells are still mainly of concern, especially for biodegradable metals. Biodegradable metals are expected to corrode over time, and their corrosion behavior over time could be highly unpredictable despite advanced techniques to control the corrosion rate, using various methods like alloying, coating, or surface modification and fabrication techniques to increase the corrosion resistance. Studies show that even permanent metals known to be inert corrode to some extent, which significantly depends on the patient’s microenvironment and

Peer review under the responsibility of KeAi Communications Co., Ltd.
* Corresponding author. Shenzhen Key Laboratory of Marine Biomaterials, CAS-HK Joint Lab of Biomaterials, Shenzhen Institute of Advanced Technology, Chinese Academy of Sciences 1068 Xueyuan Avenue, Shenzhen University Town, Shenzhen, 518055, PR China.
** Corresponding author. Shenzhen Key Laboratory of Marine Biomaterials, CAS-HK Joint Lab of Biomaterials, Shenzhen Institute of Advanced Technology, Chinese Academy of Sciences 1068 Xueyuan Avenue, Shenzhen University Town, Shenzhen, 518055, PR China.
E-mail addresses: juakim@siat.ac.cn (J. Kim), jlgilbe@clemson.edu (J.L. Gilbert), wwlu@hku.hk (W.W. Lv), ping.du@siat.ac.cn (P. Du), hb.pan@siat.ac.cn (H. Pan).

https://doi.org/10.1016/j.bioactmat.2024.11.020
Received 8 September 2024; Received in revised form 7 November 2024; Accepted 15 November 2024

inflammatory conditions, known as inflammatory cell-induced corrosion found in retrieved implant surfaces [3–5].

The corrosion of biomaterials depends on the material properties and the microenvironment (i.e., the human body), and there is mutual feedback between the implant and the cells. Innate immune cells like neutrophils and macrophages are usually the first cells to respond to foreign pathogens, including biomaterials, and they can secrete a ranging amount of reactive oxygen species (ROS) and reactive nitrogen species (RNS) [6]. Macrophages also fuse and form foreign body giant cells, adhering to the implant surface in their attempt to phagocytose the implant [7]. So, when these cells are near the implant surface and release large amounts of oxidative bursts, these oxidizing molecules directly come into contact with the implant surface, which has been reported to have adverse effects on the corrosion resistance of metals, especially for CoCrMo alloys [8]. In other words, the presence of ROS significantly reduces the impedance of the oxide films, shifting the electrode potential and increasing the corrosion rates of metals [8], making them more corrosive than otherwise known. Alternatively, all metal corrosion is a combination of oxidation and reduction reactions, and 10–15 % of the reduction reactions are found to produce some ROS [8]. Biomaterials are generally implanted in the aged, diseased, or wounded tissues rather than young and healthy, and the aged and diseased microenvironments are already highly skewed in terms of inflammation, oxidative stress, environmental pH, oxygen (i.e., hypoxia), and so on. Therefore, we may speculate that metals may not only corrode differently in aged and diseased microenvironments but also that reduction reactions from metal corrosion will affect cells significantly.

We chose to study pure Mg and Mg-Ti because, among the biodegradable metals, Mg alloys are the most popular because Mg alloys exhibit excellent biocompatibility and bioactivity and possess similar physical and mechanical properties as bone, reducing adverse effects like stress shielding, a common problem for traditional metals like CoCr and Ti alloys [9]. In addition, one of the primary reasons Mg alloys are preferred is that Mg ions are considered angiogenic and osteogenic, promoting wound healing and tissue formation. Mg ions are essential trace elements in the human body, with more than half stored in bone, and have many vital roles in the physiological functions of cells. Therefore, Mg ions released from Mg-based implants hardly raise any complications, where excess Mg ions are usually excreted via urine, and so, the incidence of Mg ion toxicity is low [10]. However, as all metal corrosion consists of oxidation and reduction reactions, so do Mg alloys. Oxidation of Mg metal involves releasing Mg ions and electrons, where Mg ions are released into solutions while electrons accumulate at the metal surface and immediately react with surrounding molecules like water and oxygen. While water and oxygen are the most abundant molecules in solutions and the atmosphere, free radicals and electrons can react with other molecules, and inside the human body, we have various biomolecules like proteins, lipids, nucleic acids, and carbohydrates with disulfide bonds and functional groups susceptible to attack, altering their structures and functions either reversibly or irreversibly [10]. Mg dissolution process involves an intermediate step where Mg is first oxidized to a monovalent Mg^+ ion, which then quickly reacts with water to produce hydrogen (H_2), hydroxides (OH^-), and Mg^{2+} ions [11].

(1) $Mg^+ \leftrightarrow Mg^{2+} + e^-$

(2) $Mg^+ + H_2O \rightarrow Mg^{2+} + OH^- + \frac{1}{2}H_2$

(3) $2H_2O + 2e^- \rightarrow 2OH^- + H_2$

Unlike water, human serum contains chloride ions, one of the major anions found (normal concentrations about 96–106 mEq/L) [12], which accelerates the corrosion of metals by breaking down the oxide film and increases the electrochemical rate [11]. For Mg alloys, the production of hydroxides increases the pH, and the buildup of hydroxides to an alkaline level higher than pH of approximately 8–9 starts to passivate the Mg surface with oxides (check Pourbaix Diagram of Mg in Ref. [9]). However, we may well consider that the initial environmental pH may start acidic or alkaline, which is the case for many pathological conditions like solid tumors, which results in acidic pH as low as 5.7–6.5 due to hypoxia [13] or in chronic wounds that result in an alkaline pH of 7.5–8.9 [14] that affects the way Mg corrodes. Oxidative stress and pro-inflammatory conditions facilitate metal corrosion, and studies found that new oxides formed in simulated inflammatory conditions were less protective of corrosion than those formed at open circuit potential (OCP), indicating that a pro-inflammatory environment affects the quality of the oxide film (i.e., passivation) [15–17]. In addition, Wiegand et al. reported that when cathodic potential was applied to CoCrMo alloy, similar to fretting corrosion conditions, large amounts of extracellular hydrogen peroxide and hydroxyl radicals were released from the metal surface, causing cell death [18,19]. So, not only do endogenous ROS produced by inflammatory cells affect the corrosion of Mg, but the immune cells also facilitate the production of exogenous ROS from the metal. The total ROS levels could significantly affect metal-cell interactions, which need to be considered, especially in conditions where excess ROS/RNS are known to be produced.

In this study, we first investigated how cells respond to Mg ions and ROS (i.e., hydrogen peroxide) in physiological or alkaline pH to see whether one particular by-product is dominating the cell behaviors or simultaneously affecting cells together. This paper shows that pH is a critical parameter that regulates cell response to Mg ions and oxidative stress, and cell viability is significantly affected not only by the pH level but also by whether the pH change is acute or chronic. Furthermore, for the first time, as far as the authors are aware, we have documented *in vitro* and *in vivo* ROS production due to active Mg corrosion (not endogenous production of ROS by cells). Hydrogen peroxide is known to modulate HIF1α, which is also proven in this study. In addition, Mg corrosion affects major signaling pathways like Wnt and PI3K/Akt/mTOR, known for BMSC proliferation and differentiation via ROS. Therefore, unlike the conventional concept that Mg alloys are osteogenic because Mg ions promote osteogenesis, ROS may also contribute to osteogenesis if ROS is produced in moderate concentrations. Lastly, Mg-Ti was fabricated via sputtering to accelerate the corrosion rate of Mg, which was increased approximately 3 times based on the hydrogen gas volume measured. While most studies attribute the cytotoxicity of Mg to a sharp increase in pH, we found that this is not the case. While alkaline pH is indeed cytotoxic, we show that Mg and Mg-Ti kill cells more quickly than NaOH-induced killing, and the cytotoxicity of Mg and Mg-Ti both follow the same pattern as that of ROS: (1) moderate levels of ROS induce cell growth arrest; (2) high levels of ROS induce cell death [20]. Overall, our study proves that reduction reactions dominate the biological responses and cell-material interactions in a corrosion rate-dependent manner, which depends on the microenvironment.

2. Materials and methods

2.1. Characterization of Mg particles

Pure Mg particles were purchased from Beijing Zhongke Yannuo New Material Technology Co., Ltd. (Beijing, China), with a purity of 99.99 % and a diameter ranging between 45 and 50 μm. 0.03 g of Mg particles were corroded in 5 mL of either phosphate buffer saline (PBS, ThermoFisher Scientific, Catalog #: 10,010,023), fetal bovine serum (FBS, ThermoFisher Scientific, Catalog #: 10,099,141), alpha-MEM (αMEM, ThermoFisher Scientific, Catalog #: 12,571,063), or complete media (αMEM + 10 % FBS + 1 % penicillin-streptomycin; PS, ThermoFisher Scientific, Catalog #: 15,140,122) for either t = 1, 3, or 7 days. Mg particles before and after corrosion were analyzed using scanning electron microscopy (SEM, Zeiss Supra® 55), energy dispersive x-ray analysis (EDX), Fourier transform infrared (FTIR, Bruker TENSOR27, software: OPUS) spectroscopy, and x-ray diffraction (XRD, Rigaku

Table 1
Mg particle concentration calculation.

Particle Weight (g)	Solution Volume to Add Particles (mL)	Mg Particle Solution (μg/mL)	Particle Solution Volume Added to the Well (mL)	Additional Solution Volume Added without Mg (mL)	Total Solution Volume per Well (mL)	Final Mg Particle Concentration per Well (μg/mL)
0.002	4	500	0.1	1.9	2	25
0.002	4	500	0.2	1.8	2	50
0.002	4	500	0.4	1.6	2	100
0.004	4	1000	0.4	1.6	2	200
0.008	4	2000	0.4	1.6	2	400
0.016	4	4000	0.4	1.6	2	800
0.032	4	8000	0.4	1.6	2	1600

ULTIMA IV, software: Jade). The particles were sputter-coated in gold for 30 s using a sputtering machine (Leica EM ACE200). SEM images were taken in secondary electron mode at an accelerating voltage of 5 kV and EDX at a higher accelerating voltage of 15 kV. *In vitro* pH was also measured for different particle concentrations of 0–1600 μg/mL using a pH microelectrode (Sentron, SI series pH probe, MicroFET 9270–010) and pH meter (Sentron, SI600) over time.

2.2. Mg particle treatment

hBMSCs were purchased from Cyagen Biosciences (HUXMF-01001; Suzhou Inc. China) at passage 2. Passage numbers 7–8 were used for all experiments. hBMSCs were cultured in complete media with αMEM as a basal media, supplemented with 10 % FBS and 1 % penicillin-streptomycin (PS; Gibco™, Catalog #: 15,140,122). Cell seeding density of 3000 cells/cm^2 was seeded in a 12-well plate (Corning, A = 3.8 cm^2, Catalog #: 3513) for 12–18 h to allow the cells to attach to the well surface.

Different concentrations of Mg particles from 0 to 1600 μg/mL were added per well, where the total solution volume was 2 mL. To yield the final concentration of 1600 μg/mL per well, 0.032 g of Mg particles were measured with a scale, then mixed immediately in 4 mL of media, yielding 8000 μg/mL particle solution. Addition of particles in solution reduced particle scattering and loss due to electrostatic forces. Large Mg particles sink in seconds if left unstirred, visible to the naked eye. So, particle solution was mixed thoroughly to yield homogeneity by pipetting up and down several times using 1000 μL micropipette before withdrawing 400 μL particle solution to add into the well. 1.6 mL of normal cell culture media was added to yield a total of 2 mL volume per well. Other particle concentrations were calculated and added in a similar manner, where the exact calculations are shown in Table 1.

hBMSCs were cultured in different Mg particle concentrations for t = 1, 2, 3, or 7 days (n = 3 samples per group). At each time point, the cell culture media and Mg particles were aspirated, and the samples were gently washed with PBS three times to remove as many Mg particles as possible before adding fresh media with 10 % CCK-8 (Sigma-Aldrich, Catalog #: 96,992) and incubated for 1 h at 37 Celsius and 5 % CO_2 before reading. Cell proliferation was measured as optical density using a microplate reader (Thermo ScientificTM MultiskanTM GO) at wavelength λ = 450 ηm. Cells were also fixed and stained to view cell

Table 2
Primer sequence list used for qPCR experiments.

Gene	Sequence (5′-3′)		Accession #	Gene	Sequence (5′-3′)		Accession #
GAPDH	Forward:	GGCTCTCCAGAACATCATCC	NM_002046.7	**MAP3K7**	Forward:	GATCGCCGGGTAGTAGGACT	NM_003188.4
	Reverse:	TTTCTAGACGGCAGGTCAGG			Reverse:	GGGGCTTCGATCATCTCACC	
WNT3A	Forward:	CAGCCACATGCACCTCAAGT	NM_033131.4	**cMYC**	Forward:	AATGAAAAGGCCCCCAAGGT	NM_002467.6
	Reverse:	GAGGCGCTGTCGTACTTGTC			Reverse:	GTCGTTTCCGCAACAAGTCC	
WNT5A	Forward:	ATTCTTGGTGGTCGCTAGGTA	XM_011534089.2	**cJUN**	Forward:	GCCAGGTCGGCAGTATAGTC	NM_002228.4
	Reverse:	CGCCTTCTCCGATGTACTGC			Reverse:	TCTGGACACTCCCGAAACAC	
DKK1	Forward:	GAGCTACCCGGGTCTTTGTC	NM_012242.4	**FOSL1**	Forward:	GTGCCAAGCATCAACACCAT	CR542278.1
	Reverse:	GGGCAGGTTCTTGATAGCGT			Reverse:	GGCTGATCTGTTCACAAGGC	
FZD10	Forward:	AGAAGAGCCGGAGAAAACCG	NM_007197.4	**CCN4**	Forward:	GTCCAGGCATGAGGTGGTT	NM_003882.4
	Reverse:	TCCCGTGGTGAGTTTTCTGG			Reverse:	CAGTGGAGCTGGGGTAAAGT	
LRP6	Forward:	AACGCGAGAAGGGAAGATGG	NM_002336.3	**PPARγ**	Forward:	GAGGACACCGGAGAGGGG	NM_138712.5
	Reverse:	CAAAGGGGCCGCTCTCAG			Reverse:	CCACGGAGCTGATCCCAAAG	
DVL1	Forward:	TACCACATGGACGAGGAGGA	AF006011.1	**SOX9**	Forward:	AGGAAGTCGGTGAAGAACGG	NM_000346.4
	Reverse:	GGTTGCTGAGCACGTTCTTG			Reverse:	CGCCTTGAAGATGGCGTTG	
DVL2	Forward:	CTGGTGAAGATCCCTGTCCC	AF006012.1	**COMP**	Forward:	CCTGCGTTCTTCTGCTCAC	NM_000095.3
	Reverse:	TTCACCACCCCGAAATCCTG			Reverse:	GCGTCACACTCCATCACC	
DVL3	Forward:	CATGGGCGAGACCAAGATCA	AF006013.1	**ACAN**	Forward:	TCAGCGGTTCCTTCTCCAG	XM_011521314.2
	Reverse:	CCCTTAAAGTCCGCCAAGGT			Reverse:	GCAGTTGTCTCCTCTTCTACG	
GSK3β	Forward:	CCTCTGGCTACCATCCTTATTC	NM_001146156.2	**PDGFRα**	Forward:	GGGCACGCTCTTTACTCCAT	NM_006206.6
	Reverse:	TTATTGGTCTGTCCACGGTCTC			Reverse:	TTAGGCTCAGCCCTGTGAGA	
β-Catenin	Forward:	TGGATTGATTCGAAATCTTGCC	XM_047447483.1	**RUNX2**	Forward:	TGCACTGGGTCATGTGTTTG	NM_001024630.4
	Reverse:	GAACAAGCAACTGAACTAGTCG			Reverse:	TGGCTGCATTGAAAAGACTG	
TCF7	Forward:	CCAAGAATCCACCACAGGAGG	NM_003202.5	**ALP**	Forward:	CCACGTCTTCACATTTGGTG	NM_000478.6
	Reverse:	GCAGCCTAGAGCACTGTCAT			Reverse:	CAGACTGCGCCTGGTAGTTG	
LEF1	Forward:	TGCCAAATATGAATAACGACCCA	NM_016269.5	**COL1A1**	Forward:	CTGGATGCCATCAAAGTCTTC	XM_054315081.1
	Reverse:	GAGAAAAGTGCTCGTCACTGT			Reverse:	AATCCATCGGTCATGCTCTC	
SMAD3	Forward:	CCTGTGCTGGAACATCATCTCAG	NM_001407013.1	**FGF2**	Forward:	AAGAGCGACCCTCACATCAA	NM_002006.6
	Reverse:	CTTCCTAAGAGTCAAAGTCCCTGC			Reverse:	ACGGTTAGCACACACTCCTT	
SMAD4	Forward:	TCTCTGGTGGAAAGGCAGAC	AB043547.1	**IL6**	Forward:	ACTCACCTCTTCAGAACGAATTG	XM_054358145.1
	Reverse:	TGAGCAAATCTCTCCCTGTCAT			Reverse:	CCATCTTTGGAAGGTTCAGGTTG	
NLK	Forward:	GACAGCTTGTGAAGGCGCTA	NM_016231.5	**HIF1α**	Forward:	CTGAGGGGACAGGAGGATCA	NM_001530.4
	Reverse:	AAAGACCAACATCCTGCAAAGG			Reverse:	CTCCTCAGGTGGCTTGTCAG	
COL10A1	Forward:	TGGGACCCCTCTTGTTAGTG	NM_001424106.1	**VEGFA**	Forward:	ACGGACAGACAGACAGACAC	NM_001025366.3
	Reverse:	TTGGGTCATAATGCTGTTGC			Reverse:	GAAGCGAGAACAGCCCAGAA	

morphology. Cells were fixed in 4 % paraformaldehyde (PFA) for 30 min and then treated with 0.2 % Triton for 10 min. Cells were stained with 1 μg/mL DAPI (Thermo-Scientific, Catalog #: 62,248) and 1:200–300 dilution of phalloidin-488 in PBS for 30 min at room temperature. Cells were imaged using JULITM stage (NanoEntek). Five images were taken per well, and based on the nucleus (DAPI), cells were counted using the "point tool" from Image J (NIH). Based on the scale bar, the area of the picture was calculated in μm^2, and the average cell number per well was used to estimate the total number of cells per well. The total cell number was then averaged from 3 samples per group.

For qPCR analysis, mRNA samples were extracted using the HiPure Total RNA Micro Kit (Magen Biotech, Catalog #: R401103) following their recommended protocol. mRNA was stored at −80 Celsius until ready to convert to cDNA. mRNA concentrations were measured using a NanoDropTM 2000/2000c spectrophotometer (Thermo-Fisher Scientific, Catalog #: ND-2000). RNA samples were used if the quality of the absorbance readings 260/280 was higher than 1.8. Reverse transcription to cDNA was performed using the reverse transcription reagent kit (PrimeScript™ Master Mix, Takara, Catalog #: RR036B). cDNA was converted using Biometra TRIO thermal cycler (Analytik Jena GmbH) in a three-step procedure: 1) 37 Celsius for 15 min, 2) 85 Celsius for 5 min, and 3) cool down to 4 Celsius for 10 min qPCR was performed using LightCycler® 96 Instrument (Roche) under repeated thermal cycling conditions of 95 Celius denaturing for 15 s and 60 Celsius annealing for 30 s. Each sample had 3-4 technical repeats, n = 3 samples per experimental group per time point. Relative quantification results were obtained by calculating the ΔΔCT and plotted in fold changes ($2^{-\Delta\Delta CT}$). The primer sequences are listed in Table 2. GAPDH was used as the housekeeping gene, and the relative gene fold was measured compared to the negative control group.

2.3. hBMSC response to Mg ions, alkaline pH, and oxidative stress

hBMSCs were cultured in the same condition as section 2.2, such as cell seeding density, passage number, and culture media, to ensure that the changes in cell behavior are only due to the treatment. hBMSCs were treated with 0–20 mM of magnesium chloride ($MgCl_2$) for t = 1, 2, 3, and 7 days. Because $MgCl_2$ contains chloride ions, which may also have a significant effect, 0–20 mM of sodium chloride (NaCl) was used as a control to ensure that the effect is solely due to Mg ions. The negative control group was hBMSCs cultured in media without $MgCl_2$ or NaCl.

hBMSCs were also treated with different alkaline pH levels, and two experiments were conducted. The first experiment involved adjusting the pH of the media to different alkaline levels of 7.75, 8, and 8.25 and changing the media every 12 h to maintain the alkaline pH level during culture time inside the incubator with 5 % CO_2 buffer. The second experiment involved adjusting the pH of the media to 7.6, 7.8, and 8 only once initially (t = 0 h) and measured the changes of the pH drop due to the 5 % CO_2 buffer. The negative control group was cells cultured in media without adjusting the pH. The main difference between the first and second experiments was the acute or chronic alkaline pH effect on cells. hBMSCs were cultured for t = 1, 2, or 3 days.

Lastly, hBMSCs were treated with either $MgCl_2$ or hydrogen peroxide (H_2O_2) at different pH levels: 7.4 or 7.75. The pH of the media was adjusted to either 7.4 or 7.75 using HCl or NaOH. Either 1 mM of $MgCl_2$, 0.44 nM of H_2O_2, or both (1 mM $MgCl_2$ + 0.44 nM of H_2O_2) were added to the media of either pH. The negative control groups were cells cultured in media with a pH of 7.4 without any addition of Mg ions or H_2O_2. There was a total of 8 groups.

1) 0 mM $MgCl_2$ + 0 nM H_2O_2 + pH 7.4
2) 1 mM $MgCl_2$ + 0 nM H_2O_2 + pH 7.4
3) 0 mM $MgCl_2$ + 0.44 nM H_2O_2 + pH 7.4
4) 1 mm $MgCl_2$ + 0.44 nM H_2O_2 + pH 7.4
5) 0 mM $MgCl_2$ + 0 nM H_2O_2 + pH 7.75
6) 1 mM $MgCl_2$ + 0 nM H_2O_2 + pH 7.75
7) 0 mM $MgCl_2$ + 0.44 nM H_2O_2 + pH 7.75
8) 1 mm $MgCl_2$ + 0.44 nM H_2O_2 + pH 7.75

The media was changed every 12 h to give multiple doses of alkaline pH with or without $MgCl_2$ or H_2O_2 to somewhat mimic the chronic alkaline and oxidative stress conditions. hBMSCs were cultured for a total of t = 1, 2, 3, or 7 days. The media was made fresh at each time point to ensure that pH did not deviate as well as the actual concentrations of $MgCl_2$ and H_2O_2.

2.4. In vitro intracellular and mitochondrial ROS measurement

Certain concentrations of Mg, 100, 400, and 800 μg/mL, were selected to measure the intracellular level of ROS. Different concentrations of H_2O_2 were used to compare the intracellular ROS levels between Mg and hydrogen peroxide. 0.1, 0.5, or 1 μL of 3 % H_2O_2 solution (ThermoFisher Scientific, Catalog #: 426,001,000) was diluted into 50 mL of cell culture media to yield the final concentrations of 0.88, 4.4, and 8.8 ηM, which were given 2 mL per well. The negative control group was hBMSCs cultured in regular cell culture media (αMEM + 10 % FBS + 1 % PS). Intracellular ROS or mitochondrial ROS were measured using the Reactive Oxygen Species Assay Kit (Beyotime, Catalog #: S0033M) or mitochondrial ROS 580 Kit (AAT Bioquest, Catalog #: 16,052) at different time points for up to 2 days of culture. Hoechst 33,342 (ThermoFisher Scientific, Catalog #: 62,249) was used to stain the live cells with ROS staining to determine whether changes in ROS reading are due to the changes in cell number or the treatment. So, the total intracellular ROS and Hoechst 33,342 were measured using three different cell seeding densities of 3000, 6000, and 9000 cells/cm^2 for calibration. ROS and Hoechst fluorescence were imaged and measured using a microplate reader (Infinite ® 200 Pro, Tecan).

2.5. In vivo ROS imaging

Balb/c nude male mice with an average weight of about 25 g were used. They were anesthetized using isoflurane gas before operation. A small cut was made subcutaneously and a pocket was created. Either 1 mm (left side) or 2 mm (right side) of pure Mg rod was inserted with 200 mL of PBS or 50 μM H_2O_2 solution to mimic the simulated inflammatory conditions. In addition, there were two blank groups without Mg but only an injection of 200 mL of PBS or 50 μM H_2O_2 solution into the pocket. The wounds were sutured, and the mice were allowed to briefly recover for 1 h. Luminol (Catalog #: HY-15922A; MedChemExpress LLC) powder was dissolved in PBS (0.01 g per ml), which was then injected into mice with a final dosage of 100 mg/kg. The bioluminescence was detected and imaged using Caliper IVIS Spectrum and Living Image® version 4.2. ROS was measured within 5–10 min after luminol injections into the peritoneum. The mice were under isoflurane anesthesia about 2–3% during imaging. ROS was measured over time at t = 1 h, 1 day, 2 days, and 3 days until there was no ROS detection. There were 3 mice per group.

2.6. Transcriptome sequencing

2.6.1. Cell preparation and experiment

Transcriptome sequencing was conducted for hBMSCs treated with either 50, 100, or 200 μg/mL of Mg for t = 1, 3, or 7 days compared to the negative control group (0 μg/mL), where at t = 7 days, only one concentration, Mg 100 μg/mL, was tested. Three samples were prepared per experimental group.

2.6.2. mRNA qualitative and quantitative analysis

After the mRNA samples were extracted, purity was assessed using Nanodrop by measuring the OD260/280 and OD260/230 ratios, and integrity was evaluated using Agilent 2100/4150.

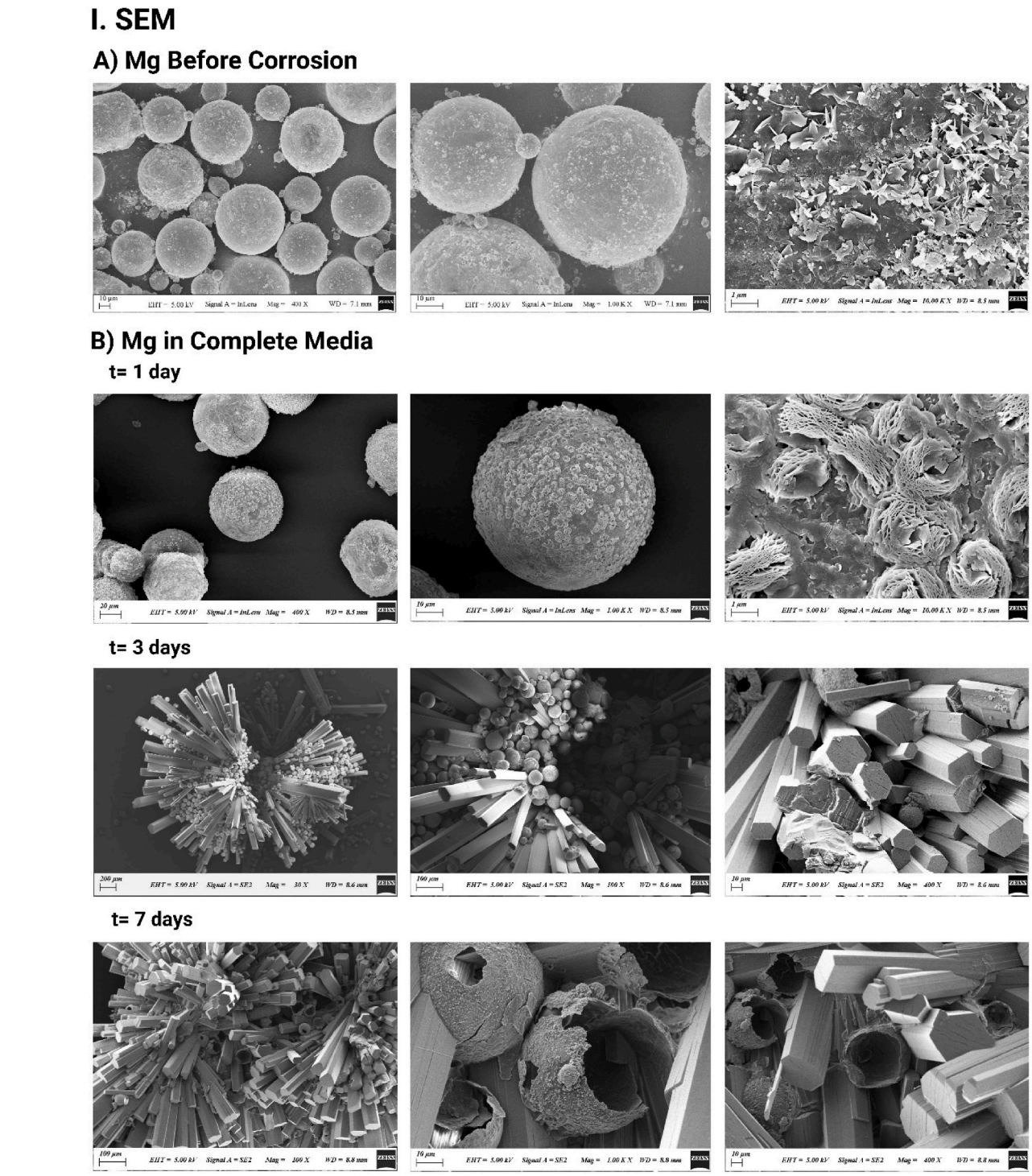

Fig. 1. A) SEM images of Mg particles before corrosion. B) SEM images of Mg particles corroded in complete media (αMEM + 10 % FBS + 1 % PS) for t = 1, 3, or 7 days. EDS showing elemental analysis for Mg particles C) before corrosion and corroded in complete media for D) t = 1 day, E) t = 3 days, and F) t = 7 days. FTIR spectrum of Mg of G) before corrosion and corroded in complete media for H) t = 1 day, I) t = 3 days, and J) t = 7 days. X-ray diffraction patterns of Mg K) before corrosion and corroded in complete media for L) t = 1 day, M) t = 3 days, and N) t = 7 days.

2.6.3. Library preparation of mRNA transcriptome sequencing

1 μg of RNA was used per sample for the mRNA library preparation. Most of the mRNA from eukaryotes had polyA tails, which were enriched by Oligo (dT) magnetic beads. The obtained mRNAs were randomly interrupted by bivalent cations, and the first strand of cDNA was synthesized in the first strand enzymes reverse transcriptase system using the segmented mRNA as the template and the random oligonucleotide as the primer. The second strand of cDNA was synthesized using the second strand of enzymes and dNTPs. Purified double-stranded cDNAs underwent end-repair, A-tailing, and ligation with sequencing adapters. cDNAs with an insert size of approximately 200–300 bps were screened. PCR amplification was performed, and the PCR product was purified again, obtaining a library. The library quality was assessed on the Agilent 4200 TapeStation.

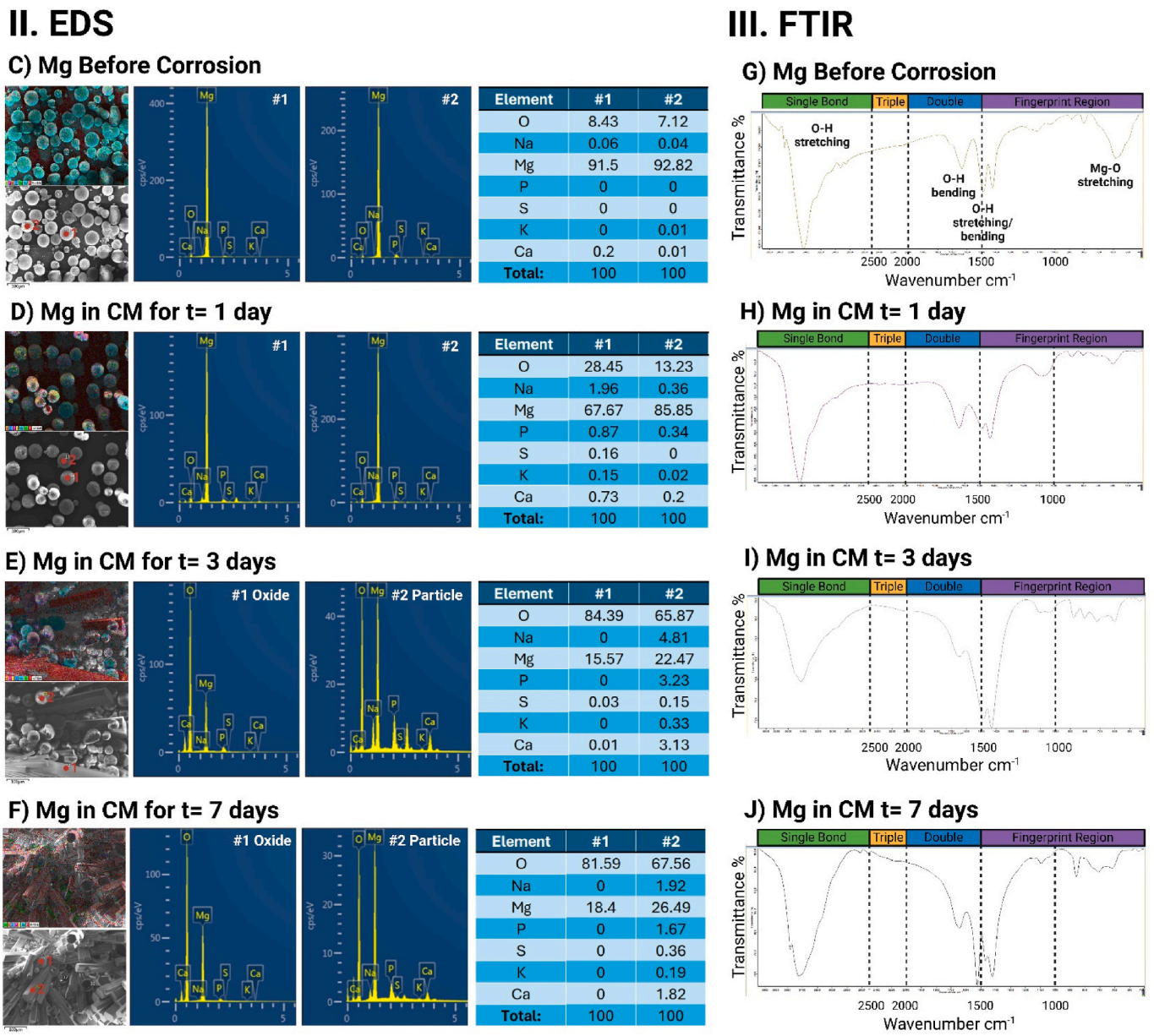

Fig. 1. (*continued*).

2.6.4. Sequencing

After passing the library inspection, the library preparations were sequenced on a NovaSeq6000 platform (CHI BIOTECH CO., LTD), and 150 bp stand-specific paired-end reads were generated.

2.6.5. DNA analysis- quality control

Raw data (raw reads) of fastq format were first processed through in-house per script. In this step, clean data (clean reads) were obtained by trimming reads containing adapter, ploy-N, or with low quality from raw data. At the same time, Q20, Q30, and GC content of the clean data were calculated. All the downstream analyses were performed based on

clean data of high quality.

2.6.6. Reads mapping to the reference genome

Reference genome and gene model annotation files were downloaded from the genome website. The reference genome index was built using Star v2.7.10b and paired-end clean reads were mapped to the reference genome.

2.6.7. Quantification of gene expression level

FeatureCounts (v2.0.3) was used to count the read numbers mapped to each gene. Then, TPM was calculated, which is the expected number of transcripts per kilobase of the exon model per million mapped reads. TPM considers the effect of sequencing depth and gene length for the read count simultaneously and is currently the most common method for estimating gene expression levels.

2.6.8. Differential expression analysis

Prior to differential gene expression analysis, for each sequenced Library, the read counts were adjusted by the EdgeR program package through one scaling normalized factor. Differential expression analysis of two conditions was performed using the EdgeR R package (3.40.2). The p-values were adjusted using the Benjamini & Hochberg method. Corrected p-values of 0.05 were set as the threshold for significantly differential expression.

2.6.9. GO and KEGG enrichment analysis of differentially expressed genes

Gene Ontology (GO) enrichment analysis of differentially expressed genes was implemented by the ClusterProfiler R (4.6.2), in which gene length bias was corrected. GO terms with corrected p-values less than 0.05 were considered significantly enriched GO functions of the gene set. KEGG is a database resource for understanding high-level functions and utilities of the biological system, such as the cell, the organism, and the ecosystem, from molecular-level information, especially large-scale molecular datasets generated by genome sequencing and other high-throughput experimental technologies (http://www.genome.jp/kegg/). We used ClusterProfiler R to test the statistical enrichment of differential expression genes in KEGG pathways.

2.7. Proteome analysis

2.7.1. Cell preparation and experiment

Proteome analysis was conducted for hBMSCs treated with 100 μg/mL of Mg for t = 2 days compared to the negative control group (0 μg/mL). Three samples were prepared per experimental group.

2.7.2. DIA (data independent acquisition)

The UltiMate 3000 (Thermo Fisher Scientific, MA, USA) liquid chromatography system was connected to the timsTOF Pro2, an ion-mobility spectrometry quadrupole time of flight mass spectrometer (Bruker Daltonik, Bremen, Germany). Samples were reconstituted in 0.1 % FA and 200 ng of peptide was separated by AUR3-15075C18 column (15 cm length, 75 μm i. d., 1.7 μm particle size, 120 Å pore size, IonOpticks) with a 60 min gradient starting at 4 % buffer B (80 % ACN with 0.1 % FA) followed by a stepwise increase to 28 % in 25 min, 44 % in 10 min, 90 % in 10 min and stayed there for 7 min, then equilibrated at 4 % for 8 min. The column flow rate was maintained at 400 ηL/min with the column temperature of 50 °C. DIA data was acquired in the diaPASEF mode. We defined 22 × 40 Th precursor isolation windows from m/z 349 to 1229. To adapt the MS1 cycle time, we set the repetitions to variable steps (2–5) in the 13-scan diaPASEF scheme. During PASEF MSMS scanning, the collision energy was ramped linearly as a function of the mobility from 59 eV at 1/K0 = 1.6 V s/cm^2 to 20 eV at 1/K0 = 0.6 V s/cm^2.

2.7.3. Database search

Raw Data of DIA were processed and analyzed by Spectronaut 18 (Biognosys AG, Switzerland) with default settings. The database was Uniprot-Homo Sapiens (version 2022, 20,610 entries), downloaded from Uniprot. Trypsin was the digestion enzyme used. Carbamidomethyl on cysteine was specified as the fixed modification. Oxidation on methionine and acetyl on protein N-term was specified as variable modification. The retention time prediction type was set to dynamic iRT. Spectronaut determined data extraction based on extensive mass calibration. Spectronaut dynamically determined the ideal extraction window depending on iRT calibration and gradient stability. The Q-value (FDR) cutoff on the precursor level was 1 %, and the protein level was 1 %. Decoy generation was set to mutate, similar to scrambled, but only applied a random number of AA position swamps (min = 2, max = length/2). The normalization strategy was set to local normalization. Peptides that passed the 1 % Q-value cutoff were used to calculate the major group quantities with the MaxLFQ method.

2.7.4. Data quality control

After the offline data from the mass spectrometry was completed, a series of quality controls were required to ensure the reliability of the data results. Quality control of mass spectrometry data included liquid phase system, mass spectrometry system, qualitative results, quantitative results, etc. The parameters of quality control included missed cleavage, specific enzyme cleavage, non-specific modification, half-peak width, ion peak time distribution, ion charge number distribution, mass axis offset, etc.

2.8. In vivo bone femur defect

Sprague-Dawley male rats with an average weight about 400–450 g were used for this study. All animal experiments were conducted at Shenzhen Institute of Advanced Technology (SIAT), Chinese Academy of Sciences (CAS), located in Shenzhen, Guangdong Province, China, under the supervision of Animal Research Committees of SIAT. Animals were kept and fed in a feeding room with a temperature of 22 Celsius and relative humidity of 40–70 %. Animals spent 7 days of an adjustment period in the feeding room before the experiment. All animals were operated on under general anesthesia (using isoflurane gas). Both femurs were drilled closer to the knee, 2 mm in size, and either pure Mg rods (diameter 2 mm x height 5 mm) were inserted or the defects were left blank. The rats were checked three consecutive days after the surgery for any signs of discomfort or perioperative infections. All animals were allowed to move, eat, and drink freely after the surgery. They were sacrificed at 1, 2, 4, or 8 weeks after implantation.

The harvested femurs from rats were fixed in 4 % paraformaldehyde (PFA, BOSTER) for 24 h at normal atmospheric temperature and then scanned with micro-CT (SkyScan 1176, Bruker, Germany) with an 18 μm resolution. NRecon software (1.7.1.0, Bruker, Germany), DataViewer (1.4.4.0, SkyScan, Germany), CT Analyser (1.11.8.0, SkyScan, Germany) were used for image format conversion, image axial adjustment, and data analysis, respectively. Using Bruker CTAn Micro-CT software, the region of interest (ROI) was chosen from the scanogram of micro-CT for threshold segmentation to analyze various morphological characteristics of the bone-implant interface and calculate new bone volume to total bone volume (BV/TV) and bone mineral density (BMD) at the femoral defect site.

Rat femurs were harvested, rinsed with PBS 3 times, and fixed with 4 % PFA for 1 day. The femur was decalcified with neutral EDTA solution for 4 weeks and dehydrated using different gradients of ethanol (70 %, 80 %, 90 %, 95 %, and 100 % volume fraction). The decalcified specimens were then sealed in a paraffin mold, which was sliced on a microtome and transferred to a slide to dry. Immunohistochemistry staining (IHC) was used to detect HIF1α and β-catenin. Image J software (NIH) and IHC Toolbox (https://imagej.net/ij/plugins/ihc-toolbox/) were used to quantify the expressions from the IHC images.

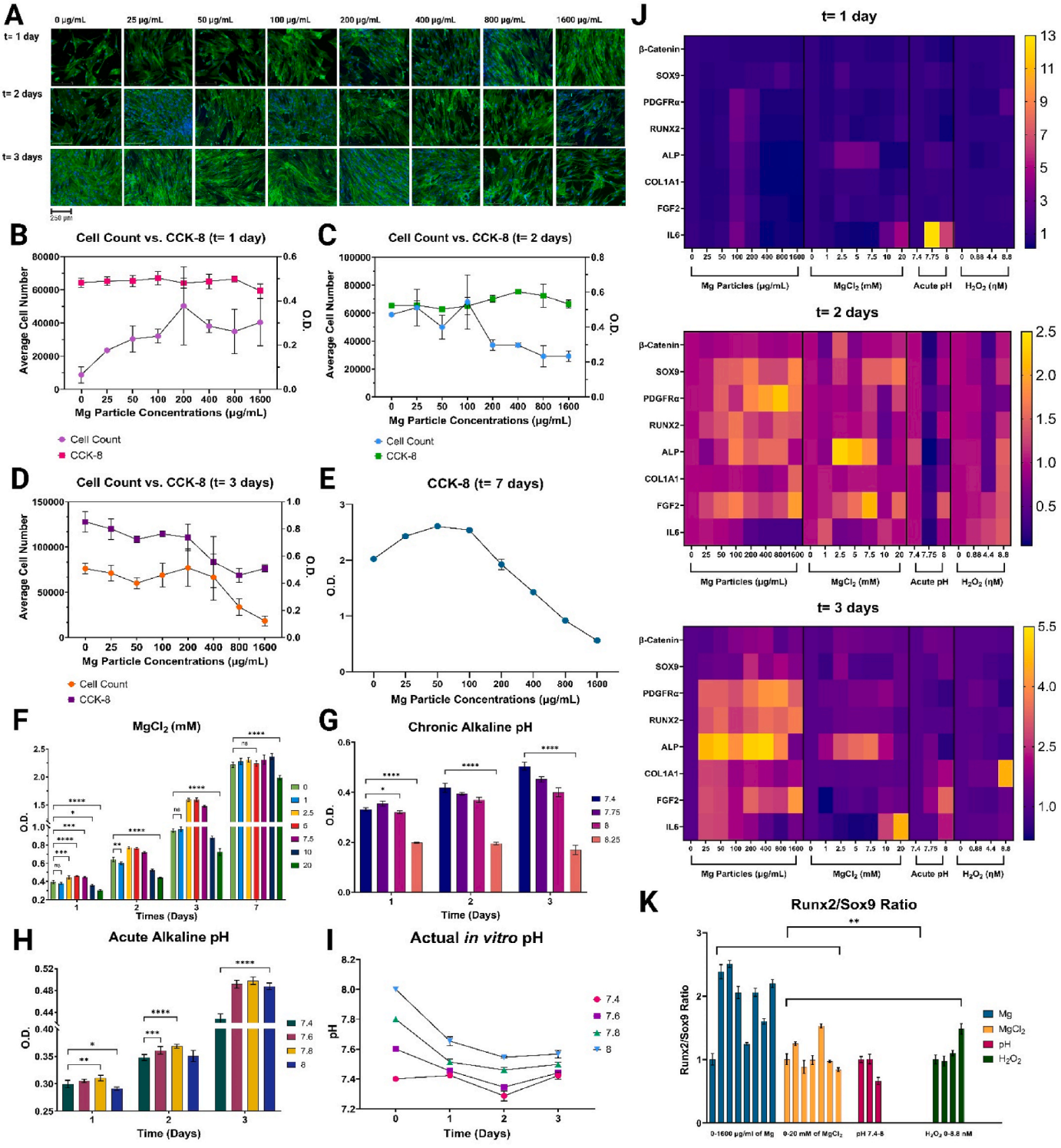

Fig. 2. A) hBMSCs treated with different concentrations of Mg particles between 0 and 1600 μg/mL, then fixed and stained with DAPI (nucleus, blue) and Phalloidin-488 (actin, green) over time t = 1–3 days. Cell count and CCK-8 analysis showing cell viability and proliferation after Mg particle treatment for B) t = 1 day, C) t = 2 days, D) t = 3 days, and E) t = 7 days (for 7 days, only CCK-8 value is shown). hBMSC proliferation shown as optical density after F) 0–20 mM of $MgCl_2$ treatment, G) chronic alkaline pH from 7.4 to 8.25 replenished every 12 h, and H) acute alkaline pH between 7.4 and 8. I) Actual *in vitro* pH measured for the acute pH experiment as the pH fell over time due to 5 % CO_2 incubation. J) qPCR measuring relative gene expressions levels for hBMSCs treated with different concentrations of either Mg particles, $MgCl_2$, alkaline pH (acute), or H_2O_2 for t = 1–3 days. K) Runx2/Sox9 ratio taken from qPCR measurements to show the potential of osteogenesis, where Mg particles showed the highest Runx2/Sox9 ratio over 2-fold compared to the other groups. Two-way ANOVA analysis was used to find statistical significance using GraphPad Prism 10.2 software, where *p < 0.05, **p < 0.01, ***p < 0.001, and ****p < 0.0001.

2.9. Mg and Mg-Ti in vitro cytotoxicity

2.9.1. Characterization of Mg and Mg-Ti particles

Mg particles were purchased from Goodfellow (Catalog #: MG006021), generated by mechanical abrasion, with 99.8 % Mg purity. These Mg particles were made from mechanical processing, such as cutting or milling. Mg particles were then sieved down to the required particle range so that most of the particles did not exceed the maximum diameter of 50 μm. These Mg particles were used to make an Mg-Ti galvanic couple via a direct current sputtering machine (Denton Vacuum Desk II, Denton Vacuum, LLC) for 5 min at 1.2 kV, 50 mA, and 100–200 mTorr. Sputtering allowed a Ti layer to cover only the top half of the Mg particles due to the line-of-sight nature of the sputtering process, leaving the bottom half of the Mg particles uncovered. The SEM images and EDS analysis of these particles are shown in Ref. [21].

Hydrogen gas volume was measured by adopting the same method as Song et al. [22]. SFig. 1 shows a schematic illustration of the experimental setup and the step-by-step pictures of the experiment for visual clarity. In short, a 5 mL pipette was used as a column to measure the hydrogen gas, where one tip was used to connect to a cone glued with silicone to prevent any gas leakage from the junctions. At the bottom of the conical funnel, 0.05 g of Mg or Mg-Ti particles were corroded in cell culture media (αMEM + 10 % FBS + 1 % PSG) to measure the hydrogen gas volume for t = 0–3 days. When hydrogen gas was produced during Mg or Mg-Ti corrosion, hydrogen gas floated up to the top of the pipette, displacing the same volume of liquid, which was recorded over time. Hydrogen gas volume was used to predict the corrosion rates of pure Mg versus Mg-Ti.

0.01 g of Mg or Mg-Ti were corroded in either 10 mL of PBS solution or 10 mL of PBS solution mixed with 2 mg/mL of fibrinogen for 4 days to understand Mg and Mg-Ti corrosion behavior in a single protein solution. XRD (Rigaku RINT2200) diffraction patterns were obtained with

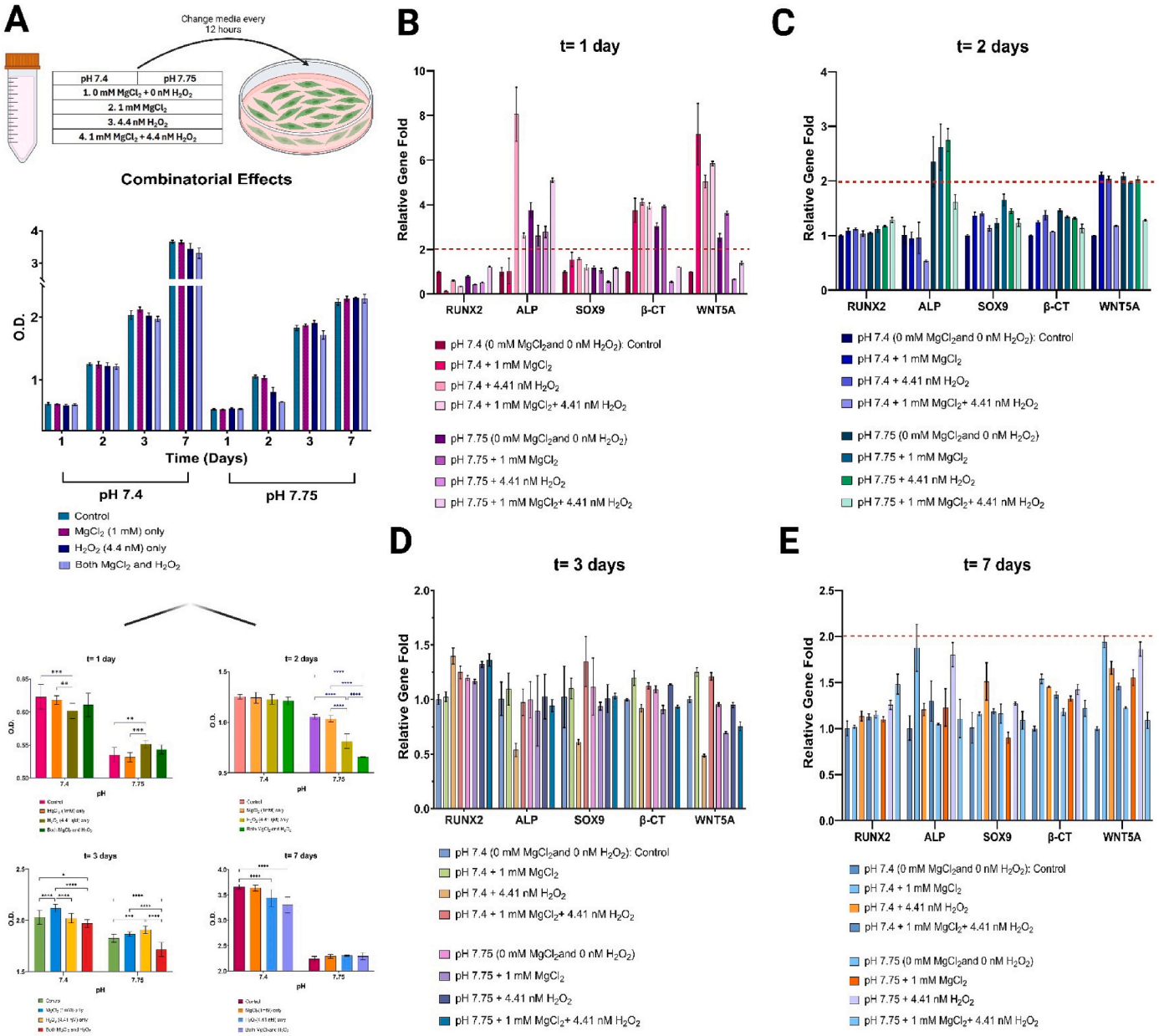

Fig. 3. hBMSCs were treated in either just Mg ions, H_2O_2, or both at either pH of 7.4 or 7.75 with media replenished every 12 h for t = 1–7 days. A) hBMSC proliferation measured in optical density and B) relative gene expressions of Runx2, ALP, Sox9, beta-catenin, and DKK1. Two-way ANOVA analysis was used to find statistical significance using GraphPad Prism 10.2 software, where *p < 0.05, **p < 0.01, ***p < 0.001, and ****p < 0.0001.

Ni-filtered Cu Kα radiation (λ = 1.54068 Å) generated at 30 kV and 30 mA at a scanning speed of 0.5°2θ/min in the range of 1-50°2θ and then analyzed using MDI (Jade version 5) software. The samples were also analyzed with FTIR (PerkinElmer Instrument and Spectrum One software) in reflectance mode, where CoCrMo alloy was used as the background sample.

2.9.2. *In vitro cytotoxicity*

Different concentrations of sodium hydroxide (NaOH, Fisher ChemicalTM, Catalog #: SS255-4) were added in 10 mL of complete media (αMEM + 10 % FBS + 1 % PSG) to vary the pH levels from 7 to 11, and the pH of the media was measured using the pH meter (Omega PHB-45, Omega Engineering, Inc.). 2 mL of complete media with different pH ranging from 7 to 11 was used to culture MC3T3-E1 (ATCC #: CRL-2593) cells with a cell seeding density of 10,000 cells/cm^2 in a 6-well

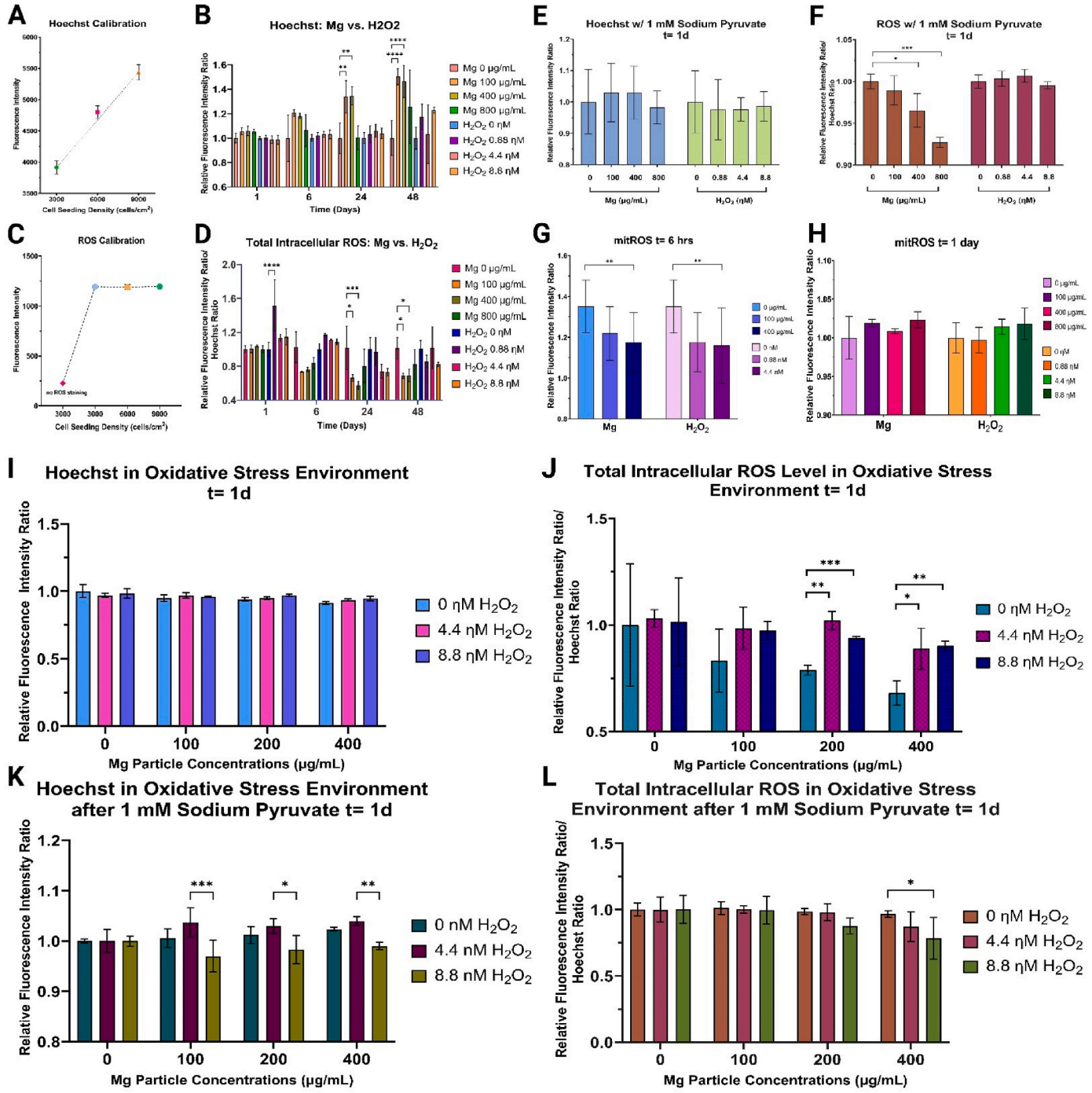

Fig. 4. A) Hoechst calibration shows that Hoechst measurement is dependent on cell numbers. B) Hoechst measurement after treating hBMSCs with either Mg 0–800 μg/mL or H_2O_2 0–8.8 ηM from 1 h to 2 days. C) ROS calibration showing ROS fluorescence intensity measurement at different cell seeding densities from 3000 to 9000 cells/cm^2. Cells at 3000 cells/cm^2 were also measured without ROS staining. E) Hoechst and F) total intracellular ROS levels after Mg or H_2O_2 treatment and 1 mM sodium pyruvate for t = 1 day. I) Hoechst and J) total intracellular ROS levels after Mg particle treatment in oxidative stress environment for t = 1 day. K) Hoechst and L) total intracellular ROS levels after Mg particle treatment in oxidative stress environment with 1 mM of sodium pyruvate for t = 1 day. Two-way ANOVA analysis was used to find statistical significance using GraphPad Prism 10.2 software, where *p < 0.05, **p < 0.01, ***p < 0.001, and ****p < 0.0001.

plate (A = 9.6 cm^2 per well) for either t = 1 h or t = 1 day. MC3T3-E1 cells were also cultured with Mg or Mg-Ti 0–1750 μg/mL for either t = 1 h or t = 1 day. Certain concentrations of Mg (250, 750, and 1500 μg/mL) were used to treat MC3T3-E1 over time from t = 0 h to 72 h. At the end of the desired time point, cells were stained with live/dead assay (InvitrogenTM, catalog #: L3224) to measure cell viability. Ten images were randomly taken per sample, 3 samples per group (30 images per group). Cell viability was measured as % cell viability = # live cells/(# live cells + # dead cells) * 100 %. Cells were counted using the "cell counter" tool from the Image J software (NIH).

2.10. Graphs and statistical analysis

Either one-way or two-way ANOVA analysis was used in GraphPad Prism 10 software to measure significance, where *p < 0.05, **p < 0.01, ***p < 0.001, and ****p < 0.0001. All graphs were generated from GraphPad Prism 10, and all illustrations and images were generated using BioRender (https://www.biorender.com).

3. Results

According to Fig. 1, Mg particles purchased from Beijing Zhongke Yannuo New Material Technology Co. Ltd. Were spherical in shape with smooth surfaces, yielding a moderate corrosion rate in solution, although the purity of Mg was high (99.99 %). The average diameter of Mg particles was 45–50 μm, achieved by mechanical sieving, but there was still 5–15 % fine powder with a smaller diameter range between 5 and 15 μm (Fig. 1A). Regardless, the size of these Mg particles was in a narrow range that achieved relatively consistent and uniform corrosion rate and duration, where most of these particles actively corroded for 2–3 days. Furthermore, the size ranges of these particles were equivalent or larger than an average hBMSC and so, large microparticles were used to ensure that cell-material interactions are mostly extracellular and electrochemical, minimizing any individual phagocytosis via the lysosomal pathway and causing some kind of genotoxicity due to particle internalization. This was particularly true when assessing cells in the early time points within 24–48 h. While we did not assess genotoxicity and effect of particle internalizations in this study, there is a study by Di Virgilio et al. that used magnesium particles (purity 99.8 %) with an average size of 58.9 μm ± 20.7 μm that measured cytotoxicity and genotoxicity [23]. For their study, rat osteosarcoma UMR106 cells treated with magnesium particles for 24 h showed a positive micronucleus test that showed chromosomal damage in a concentration-dependent manner, as well as DNA strand breaks using Comet assay for those treated with particle concentrations of 500 μg/mL. Since our study design is similar, we also expect that the cells could have internalized the particles, and at high concentrations, some genotoxicity is induced. In our study, Mg particles were randomly distributed in solutions during corrosion, so particle corrosion might not have been homogeneous in areas where particles were more clumped, preventing even particle exposure to the solution. So, some particles were corroded completely with a thick formation of oxides; in contrast, others remained partially or largely uncorroded, leading to some variability in individual particle corrosion. High particle concentrations increased particle aggregation that led to oxide needle formation seen in SEM images, but oxide needles did not form in cell experiments for the particle concentrations between 0 and 1600 μg/mL.

Despite this limitation, SEM and EDS analysis showed that Mg particles corroded well in complete media, forming needle-shaped oxides over time (Fig. 1B). EDS analysis of Mg particles before corrosion consisted mostly of Mg (more than 90 %) (Fig. 1C), although there was a slight oxidation due to long-term storage (about 2 years) and exposure to oxygen in the atmosphere despite careful sealing and storage (see SFig. 2). Mg particles corroded quickly during the first three days, where Mg content reduced to 15–22 % while O content increased to 65–85 %, indicating oxide or hydroxide formation on the Mg surface (Fig. 1D–F). There was a distinct difference in other elemental content between oxide/hydroxide films and the remaining Mg metal surface, where the oxide/hydroxide consisted of only Mg and O, while the remaining Mg metal also contained some Na, Ca, and P. FTIR analysis also indicated that Mg particles before corrosion did have some oxidation, showing a strong and broad band around 3200-3500 cm^{-1}, associated with -OH stretching vibration of surface-adsorbed water molecules [24], which exist in all groups (Fig. 1G–J). Two regions showed high variability between before and after corrosion; the first was the low-frequency fingerprint region around 850-550 cm^{-1}, corresponding to the stretching vibration of Mg-O bonds specific to the material [24]. This region showed up as a sharp peak for Mg powder before corrosion but disappeared for those corroded in complete media (CM), possibly showing that MgO formed from atmospheric oxidation converted to stable Mg $(OH)_2$ in solution. Another region that exhibited changes was between 1400 and 1500 cm^{-1}. Twin peaks that appeared in Mg particles before corrosion increased in intensity and sharpness for those corroded in CM, also correlating to -OH stretching and bonding [25,26], another indication of $Mg(OH)_2$ formation rather than MgO. XRD provided further insight into the changes in surface crystallography due to the corrosion of Mg. First, Mg before corrosion shows peak diffraction patterns that match the XRD of pure Mg found in other literature [27]. XRD analysis showed a peak at 18°, referring to $Mg(OH)_2$ (001), which showed up after the corrosion of Mg in CM for t = 7 days. There were four peaks between 25 and 30° that could not be immediately explained because they did not seem to belong to either pure Mg, MgO, or $Mg(OH)_2$; however, there is a hypothesis that these are unique peaks that indicate some crystallography on the Mg surface due to the presence of proteins that affected Mg corrosion and oxidation since these peaks only appeared when Mg particles were corroded in either FBS, αMEM, or CM but not in PBS (SFig. 6). SFigs. 2–7 provide detailed material characterization (SEM, EDS, FTIR, and XRD) and *in vitro* pH measurements of Mg particles corroded in different solutions, mainly PBS, FBS, αMEM, or CM over time, to show that Mg corrosion is significantly affected by the presence of proteins (i.e., FBS), causing passivation. The *in vitro* pH levels of even the highest concentrations, like 1600 μg/mL of Mg particles, did not exceed 8.2 at t = 0 h, which drops to 7.5 after t = 3 h in 5 % CO_2 incubation, indicating that the corrosion rate is not high (SFig. 7).

hBMSCs were treated with different Mg particle concentrations between 0 and 1600 μg/mL for t = 1, 2, 3, and 7 days to understand how different corrosion rates of Mg, mimicked by particle concentrations, affect cells over time (Fig. 2A–E). CCK-8 analysis showed no significant changes in cell proliferation for the first two days; however, based on cell images, there seemed to be a difference in cell number between groups (Fig. 2A–C). Therefore, cells were manually counted per image to estimate the average cell number per well and some discrepancies in the cell number data and CCK-8 in the first two days (Fig. 2C and D). For instance, CCK-8 analysis shows that cell proliferation did not change at t = 1 day, but the average cell numbers increased proportionally to increasing particle concentrations, with the average cell numbers around 10,000 cells (per well) from the control group (0 μg/mL) and about 40,000 cells for the 1600 μg/mL group at t = 1 day, showing about a 4-fold increase in cell numbers due to particle treatment, even though the cell seeding density was the same (3000 cells/cm^2) (Fig. 2B). The early corrosion phase promoted cell proliferation. Similarly, at t = 2 days, CCK-8 analysis shows almost no changes, but there was a significant decrease in cell viability as particle concentrations increased, which is the opposite of the first day (Fig. 2C). Based on the cell count, cell numbers more or less decreased proportionally to increasing particle concentrations, with average cell numbers (per well) for the control and 1600 μg/mL about 60,000 and 35,000 cells at t = 2 days, respectively. At t = 3 days, CCK-8 analysis and cell count matched as Mg corrosion was significantly reduced and almost finished. The average cell numbers for the 0 and 1600 μg/mL are about 80,000 and 25,000, respectively, and the average O.D. values for the 0 and 1600 μg/mL are about 0.8 and 0.5, respectively (Fig. 2D). The discrepancy between CCK-8 and cell count in

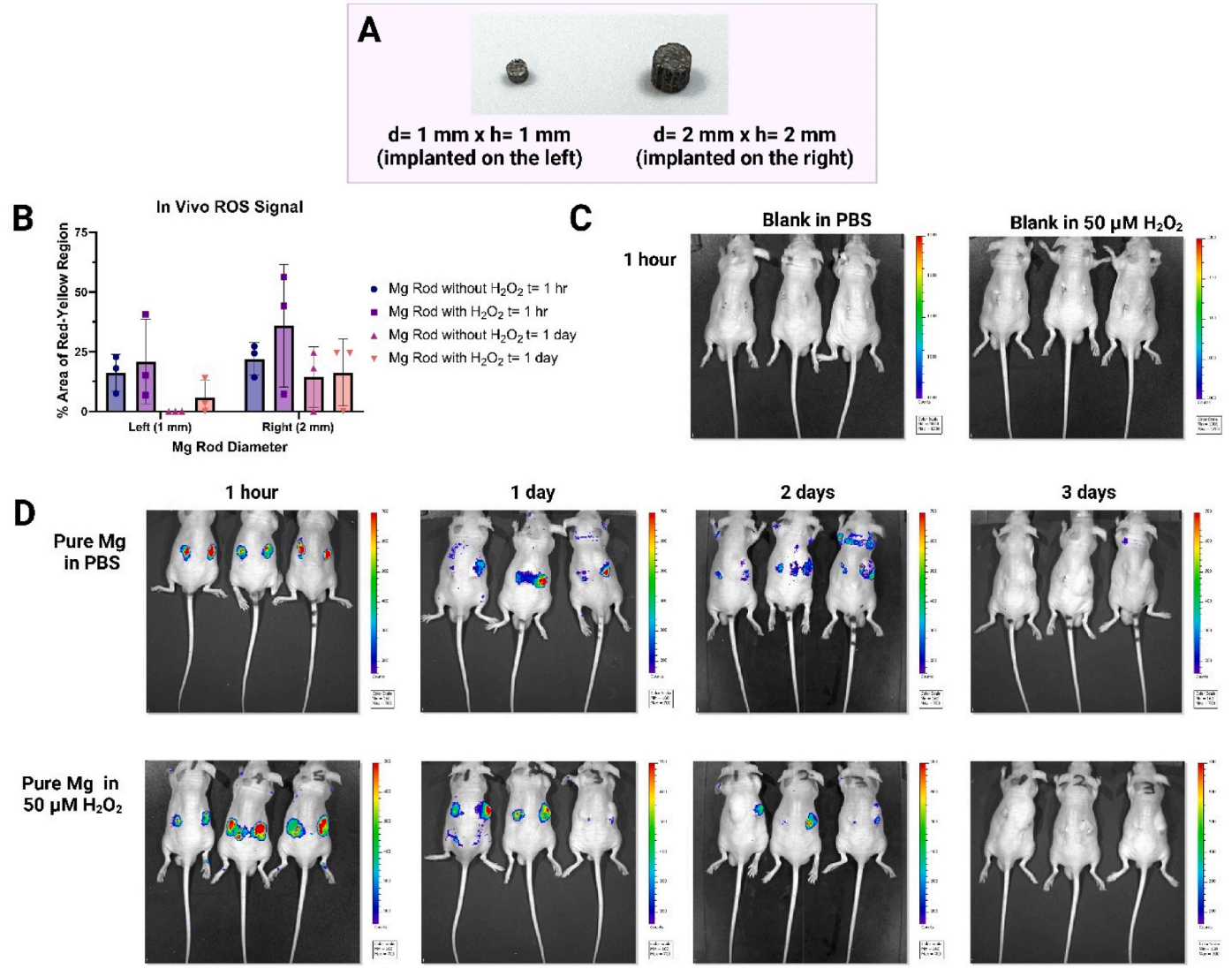

Fig. 5. A) Mg implant rods that were implanted in Balb/c nude mice. Two different sizes of Mg were implanted in the same mice. B) Total intracellular ROS signals detected after implantation of either 1 mm (left) and 2 mm (right) diameter pure Mg rods subcutaneously in mice for either t = 1 h or 1 day. Images of C) blank controls without Mg rods, either injected with PBS or 50 μM H_2O_2 into the subcutaneous pocket (about 200 mL of volume) to show that without Mg rods, there is no ROS detection. D) Pure Mg rods were inserted with either PBS or 50 μM H_2O_2 solution over time from 1 h to 3 days until no ROS signal was detected. The min and max thresholds used to detect for blank groups were min = 1000 and max = 1200 and for Mg groups min = 160 and max = 700. Two-way ANOVA analysis was used to find statistical significance using GraphPad Prism 10.2 software, where *$p < 0.05$, **$p < 0.01$, ***$p < 0.001$, and ****$p < 0.0001$.

the first two days can be explained by the fact that Mg corrosion interferes with the reduction of WST-8 molecule that typically yields yellow-colored formazan that reflects the dehydrogenase activity of living cells, where the yellow color is measured as optical density. While our experimental protocol involved gently washing the cells 3–4 times with PBS to remove as many Mg particles as possible before adding a fresh media with 10 % CCK-8 and incubating for t = 1 h before reading, not all Mg particles could be ideally removed as some Mg particles remain entangled with cells. However, longer culture times like t = 7 days were not affected because Mg particles were corroded entirely and oxidized before this time point (data not shown; based on SEM or microscopical images, as well as changes in pH). Therefore, actual cell count may be a more reliable measurement of cell viability when any metal is actively corroding. At t = 7 days, which is the post-corrosion period, lower concentrations between 25 and 100 μg/mL significantly increased cell proliferation compared to the control group, while higher concentrations between 200 and 1600 μg/mL showed significantly lower viability than the control group (Fig. 2E). Another way of viewing the data is that all Mg groups except 1600 μg/mL were able to proliferate over time by t = 7 days, showing an increase in the O.D. values over time; however, there were no significant changes in the O.D. values for the Mg 1600 μg/mL group from t = 1 day to 7 days. The average cell numbers are more or less around 40,000 for the first two days and about 25,000 at t = 3 days. The O.D. values for t = 3 and 7 days are about 0.5 at both times, showing that at this high concentration, cells cannot proliferate, indicating cytotoxicity. We also repeated the experiment with a higher cell seeding density of 10,000 cells/cm^2, provided in SFig. 8; toxicity measurement is significantly affected by cell seeding density, but gene expressions were relatively the same (showing the same trend of either up or down-regulation).

Next, we investigated how Mg ions ($MgCl_2$), H_2O_2, and alkaline pH (NaOH) affected hBMSCs independently before investigating how they affected cells concomitantly. We wanted to investigate whether the initial increase in cell number at t = 1 day is due to Mg ions or some other factor. Mg ions induced high cell proliferation for intermediate concentrations between 2.5 and 7.5 mM compared to the control group,

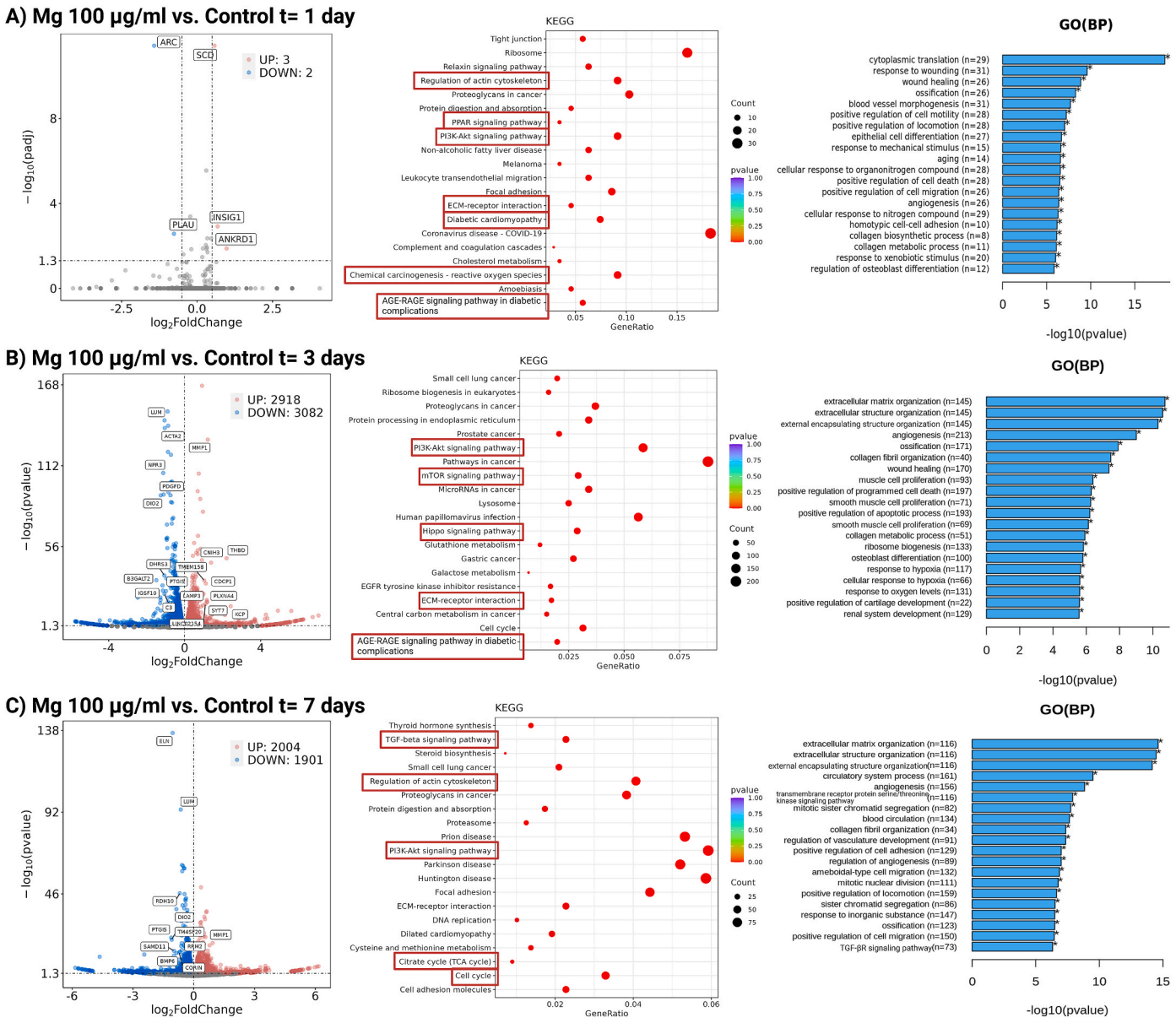

Fig. 6. Transcriptome sequencing of hBMSCs treated with Mg 100 μg/mL for A) t = 1 day, B) t = 3 days, and C) t = 7 days compared to the control group (no particle treatment). KEGG pathway analysis shows that pathways enriched include PI3K/Akt pathway for all time points. Other enrichment pathways include ECM-receptor interaction, AGE-RAGE signaling pathway in diabetic complications, TGF-beta signaling pathway, cell cycle/citrate cycle, chemical carcinogenesis-reactive oxygen species (ROS).

as early as t = 1 day (Fig. 2F). By t = 3 days, Mg ions 2.5–7.5 mM increased cell proliferation by 1.5-fold. Cell proliferation was much slower for the 10- and 20-mM groups in the first three days, but cells were still able to proliferate and reach confluency by t = 7 days. This dose-dependent response to Mg ions was actually observed when cells were treated with Mg particles for t = 7 days. Cells treated with Mg particles of 25–100 μg/mL showed significantly increased cell proliferation compared to the control group, where the O.D. values were around 2 and 2.5–2.8 for the control and 25–100 μg/mL groups, respectively. A hypothesis is that during the first three days, Mg particles were actively corroding, so the cell viability was affected more by the reduction reactions than by Mg ions. However, at t = 7 days, when most of the Mg particles stopped corroding, reduction reactions also stopped, and so, Mg ions released into the solution were able to promote cell proliferation. Interestingly, 25–100 μg/mL of Mg particles would theoretically release about 1–4 mM of Mg ions if particles were completely corroded, which aligns with the concentrations of Mg ions found to enhance cell proliferation (2.5–7.5 mM). To ensure that Mg ions are inducing proliferation and not chloride ions, we compared the $MgCl_2$ with NaCl in SFig. 9. Since there are 1:2 chlorides in NaCl:$MgCl_2$, 2.5 mM of NaCl was compared to 5 mM of $MgCl_2$, for example. While $MgCl_2$ shows a significant increase in cell proliferation, NaCl does not, so we can attribute the enhanced proliferation to Mg ions.

Chronic alkaline pH (Fig. 2G) and acute alkaline pH (Fig. 2H) were similar in experimental design, except for the duration. Cells in the acute alkaline pH experiment were cultured in cell culture media with pH adjusted only at t = 0 h, which drifted over time until the end of the experiment due to a 5 % CO_2 buffer. The actual *in vitro* pH levels were measured in Fig. 2I; for example, pH 8 at t = 0 h shifted to pH 7.7 after 1 day. Acute alkaline pH increased cell viability significantly by t = 3 days for all alkaline pH groups. Previous studies that reported that moderate alkaline pH is beneficial to osteoblast and BMSC proliferation and activity used this acute pH method [28–31], coinciding with our results. On the other hand, chronic pH shows the opposite trend. This

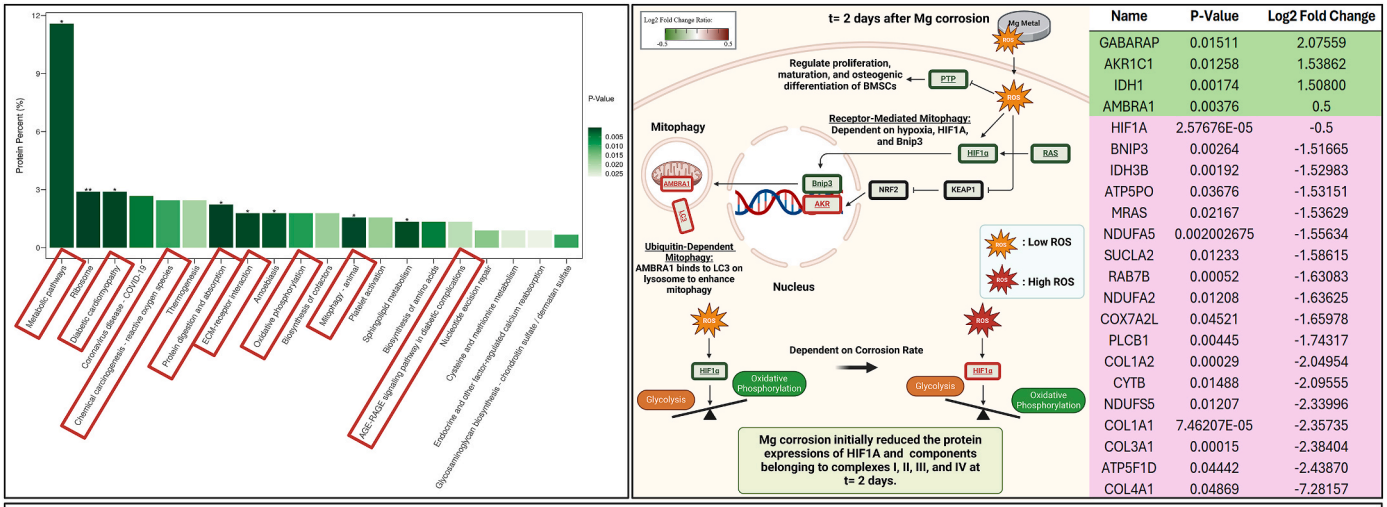

Name	P-Value	Log2 Fold Change
GABARAP	0.01511	2.07559
AKR1C1	0.01258	1.53862
IDH1	0.00174	1.50800
AMBRA1	0.00376	0.5
HIF1A	2.57676E-05	-0.5
BNIP3	0.00264	-1.51665
IDH3B	0.00192	-1.52983
ATP5PO	0.03676	-1.53151
MRAS	0.02167	-1.53629
NDUFA5	0.002002675	-1.55634
SUCLA2	0.01233	-1.58615
RAB7B	0.00052	-1.63083
NDUFA2	0.01208	-1.63625
COX7A2L	0.04521	-1.65978
PLCB1	0.00445	-1.74317
COL1A2	0.00029	-2.04954
CYTB	0.01488	-2.09555
NDUFS5	0.01207	-2.33996
COL1A1	7.46207E-05	-2.35735
COL3A1	0.00015	-2.38404
ATP5F1D	0.04442	-2.43870
COL4A1	0.04869	-7.28157

Signaling Pathway	P-Value	Ratio Tested	Matching Genes
Metabolic pathways	0.001310301	52/449	B4GALT5 | **NDUFA2** | IDH3B | **NDUFS5** | PDE8A | **IDH1** | **CYTB** | DHFR | PNP | UROD | CKM | HEXA | GSTA1 | PYGM | SMPD1 | IMPDH1 | TKT | ATP5F1D | MAT2A | TALDO1 | BTD | STT3A | **ATP5PO** | GCLC | PCYT1A | ALDH5A1 | GALC | PTS | **AKR1C1** | ASAH1 | **NDUFA5** | PGM2L1 | NAPRT | COX15 | CA13 | GALNT11 | SGMS2 | SDSL | MARS2 | APIP | SCLY | NSD1 | NMNAT1 | **PLCB1** | NANS | AGPAT3 | PIGV | **SUCLA2** | B4GALT7 | DSE | **COX7A2L** | GANC
Diabetic cardiomyopathy	0.00051333	13/449	**NDUFA2** | **NDUFS5** | **CYTB** | **COL1A1** | **COL3A1** | **COL1A2** | CPT2 | **ATP5F1D** | PPP1CC | **ATP5PO** | **NDUFA5** | **PLCB1** | **COX7A2L**
Chemical carcinogenesis - reactive oxygen species	0.010063411	11/449	**NDUFA2** | **NDUFS5** | **CYTB** | GSTA1 | **ATP5F1D** | **ATP5PO** | **AKR1C1** | PTPRJ | **HIF1A** | **NDUFA5** | **COX7A2L**
Protein digestion and absorption	8.48126E-05	10/449	**COL1A1** | **COL3A1** | **COL4A1** | ATP1B1 | COL5A2 | **COL1A2** | COL11A1 | COL5A1 | PRSS3 | COL16A1
Oxidative phosphorylation	0.009191255	8/449	**NDUFA2** | **NDUFS5** | **CYTB** | **ATP5F1D** | **ATP5PO** | **NDUFA5** | COX15 | **COX7A2L**
ECM-receptor interaction	0.000671178	8/449	**COL1A1** | **COL4A1** | FN1 | **COL1A2** | TNC | SDC4 | ITGA1 | HSPG2
Mitophagy - animal	0.000970235	7/449	**MRAS** | **GABARAP** | **BNIP3** | **HIF1A** | **RAB7B** | CITED2 | **AMBRA1**
Autophagy - animal	0.035086544	7/449	**MRAS** | **GABARAP** | **BNIP3** | **HIF1A** | **RAB7B** | C9orf72 | **AMBRA1**
AGE-RAGE signaling pathway in diabetic complications	0.021271571	6/449	**COL1A1** | **COL3A1** | **COL4A1** | FN1 | **COL1A2** | **PLCB1**
Citrate cycle (TCA cycle)	0.027020457	3/449	**IDH3B** | **IDH1** | **SUCLA2**

Fig. 7. Proteome analysis after Mg treatment for t = 2 days. Enriched pathways found in proteome analysis matched enrichment pathways found from transcriptome sequencing, including chemical carcinogenesis- ROS, mitophagy, AGE-RAGE, citrate cycle, ECM-receptor interactions, and so forth.

experiment should have ideally exposed cells to a fixed alkaline pH, but this was impossible with our current available resources. So, instead, the media was changed every 12 h to maintain the alkaline pH as much as possible, although this method is imperfect in that the media could also drift in between the 12 h. However, despite the limitations of the current method, some observations were made. When cells were exposed to chronic alkaline pH (or "multiple doses" of alkaline pH), cell viability was adversely affected even if the pH was not too high. Specific gene expressions were measured and compared among those treated with Mg particles, $MgCl_2$, acute alkaline pH, and H_2O_2, and Mg particles were the only group that was able to significantly up-regulate (more than 2-fold) genes like RUNX2, FGF2, and PDGFRα when other groups could not (Fig. 2J). FGF2 and PDGFRα are both critical for angiogenesis, bone healing and remodeling [32–36]; RUNX2 is a master transcription factor essential for osteogenesis [37], and so it is interesting that these genes are only up-regulated by Mg corrosion. Mg ions and Mg particles both up-regulated ALP gene expression important for osteoblast activity and bone mineralization [38]; however, Mg ions at high dosage also up-regulated IL-6, a pro-inflammatory gene [39] at t = 3 days. IL-6 was also significantly up-regulated at t = 1 day due to acute alkaline pH; however, Mg particles never up-regulated IL-6 even at high particle concentrations. In fact, Mg particles significantly down-regulated down to 0.5 or lower with increasing concentrations at t = 2–3 days. Pricola et al. have shown that BMSCs normally secrete a substantial amount of IL-6, but IL-6 production is significantly reduced during their differentiation into osteogenic cells [40]. So, Mg corrosion may be promoting osteogenic differentiation of hBMSCs *in vitro*, reducing IL-6 expression. Overall, Mg particles were the only group that up-regulated genes related to osteogenesis and angiogenesis like Runx2, FGF2, PDGRFα, ALP, and COL1A1 at t = 3 days, while down-regulating IL-6. In particular, the Runx2/Sox9 gene expression ratio [41], known as a good indicator of the osteogenic potential of MSCs, was measured to show that only the Mg particle group showed a ratio higher than 2-fold (Fig. 2K), while Mg ions and H_2O_2 groups could only increase by 1.5-fold, and alkaline pH significantly reduced the Runx2/Sox9 ratio when pH was at 8.

We also investigated the combinatorial effect of Mg ions, alkaline pH, and H_2O_2. Chronic alkaline pH reduced the overall viability of all groups compared to physiological pH. However, some notable observations could be made. First, at t = 2 days, cell proliferation of all groups at pH 7.4 was the same (Fig. 3A). However, at chronic alkaline pH of 7.75, cells treated with H_2O_2 or both $MgCl_2$ and H_2O_2 showed significant reduction (around 1 for the control group, around 0.8 for H_2O_2 only, and around 0.6 for both; about 20–40 % reduction in proliferation). In contrast, at t = 7 days, cells treated with H_2O_2 only or both $MgCl_2$ and H_2O_2 showed a significant decrease in cell proliferation (around 3.7 for the control group, around 3.4 for H_2O_2 only, and around 3.3 for both; about 10 % reduction in proliferation). So, in summary, cells exposed to chronic alkaline pH show a lower viability than those cultured at a pH of 7.4; however, cells exposed to chronic oxidative stress at a pH of 7.4 eventually lead to a lower viability than those cultured in non-oxidative stress of the same pH, while cells exposed to chronic oxidative stress at alkaline pH show no difference compared to those cultured in alkaline pH alone. This means that at alkaline pH, oxidative stress has no influence on cell viability/proliferation. Chronic alkaline pH significantly up-regulated certain genes that acute alkaline pH could not, especially at t = 1 day, such as WNT5A, β-catenin, and ALP (Fig. 3B). For the ALP gene, cells treated with H_2O_2 or both $MgCl_2$ and H_2O_2 at pH of 7.4 and all

groups in alkaline pH of 7.75 showed a significant up-regulation at t = 1 day. At t = 2 days, ALP gene remained up-regulated for those cultured in alkaline pH (Fig. 3C). For the β-catenin gene, all groups except those treated with H_2O_2 or both $MgCl_2$ and H_2O_2 at alkaline pH showed significant up-regulation at t = 1 day, and WNT5A showed the same trend as β-catenin, possibly because WNT5A is the upstream gene that activates β-catenin in the WNT signaling pathway.

Lastly, we measured total intracellular ROS and mitochondrial ROS after treating cells with either Mg particles, H_2O_2, or Mg particles in H_2O_2 to mimic simulated inflammatory conditions. We selected 0–8.8 ηM H_2O_2 concentrations to mimic simulated inflammatory conditions because any concentrations higher than 8.8 ηM H_2O_2 began to significantly decrease cell viability (for this cell type and cell seeding conditions), and we did not want the H_2O_2 itself to affect cell viability (not shown). Hoechst was first calibrated by measuring the fluorescence intensities for cells at different cell seeding densities from 3000 to 9000 cells/cm^2, which showed that Hoechst depends on the live cell number (Fig. 4A). Hoechst fluorescence intensity is divided by that of the control group at t = 1 h to show relative fluorescence intensity. Unlike H_2O_2 groups, Mg treatment slightly increased cell numbers after 24–48 h of culture, which is consistent with the cell count data in Fig. 2 (Fig. 4B). Total intracellular ROS was also calibrated by measuring the fluorescence intensities at different cell seeding densities (Fig. 4C). The ROS signal was also measured without the ROS staining to ensure that the ROS kit gives positive signals. When cells were cultured without any treatment, ROS levels did not vary even if the cell seeding density increased up to 3-fold, meaning that there won't be any significant changes in the ROS measurement due to cell number. Total intracellular ROS levels were then measured after Mg or H_2O_2 treatment, and the fluorescence intensities were not only divided by that of the control group to show relative changes but also divided by the fluorescence intensity ratio from the Hoechst experiment (Fig. 4B) in order to calculate the total intracellular ROS levels detected per cell instead of per well (Fig. 4D). It was interesting to observe that the Mg groups of 100 and 400 μg/mL that enhanced cell proliferation at 24–48 h exhibited a significant decrease in total ROS levels, where the relative ROS levels measured were 1 for the control and 0.5–0.6 for the Mg groups (about 40–50 % reduction).

It was impossible to tell which specific ROS level was changing due to the treatment, so we repeated the experiment for the t = 1 day group and added 1 mM of sodium pyruvate, known to reduce hydrogen peroxide into water, acetate, and carbon dioxide [42]. While Mg particles without sodium pyruvate significantly increased the Hoechst measurements at t = 1–2 days, the addition of sodium pyruvate showed no changes (Fig. 4E), further supporting that significant increase in cell proliferation during early corrosion of Mg may be due to ROS, not Mg ions. The total intracellular ROS due to Mg particles still decreased with increasing particle concentrations, but the relative changes were far less, from 1 (0 μg/mL) to 0.97 (400 μg/mL) in the presence of sodium pyruvate, while total ROS levels decreased far more from 1 to 0.5 without sodium pyruvate (Fig. 4F). However, cells treated with H_2O_2 showed no significant changes in Hoechst nor total ROS with or without sodium pyruvate, possibly because H_2O_2 by itself in this concentration range does not show any effect, especially when half-life is in milliseconds [43]. We also measured mitochondrial ROS to see if the reduction in total ROS is due to mitochondria (Fig. 4G and H). The purpose was to see

Table 3
Differential Genes Expressed by hBMSCs treated with Mg 100 μg/mL [44–84].

Time Cultured	Log2 Fold Change	P-Value	Adj. P-Value	Gene	Gene Function	Ref.
t= 1 day	0.68314991	3.425E-07	0.00120715	INSIG1	INSIG1 maintains glucose homeostasis; can up-regulate Runx-2 through the AMPK pathway. Deficiency in INSIG1/2 disrupts bone formation and homeostasis.	[44-45]
	0.580266798	4.248E-16	3.743E-12	SCD	SCD regulates the expressions of genes involved in lipogenesis and mitochondrial fatty acid oxidation. Silencing of SCD-1 suppressed osteogenesis by down-regulating osteogenic genes and ALP activity. miRNA-429 are upregulated in osteoporotic patients or under oxidative stress and mediate osteogenesis via down-regulation of SCD-1.	[46]
	0.306823307	4.801E-10	2.8204E-06	MYH9	Participates in generation of intracellular chemo-mechanical forces and translocation of actin cytoskeleton. Secreted osteoblast-derived extracellular vesicles were isolated from mineralizing osteoblasts, which propagate mineralization of bone, and found that MHY9 is one protein enriched during the first week.	[47-48]
	-0.22403247	9.46E-08	0.0004168	TIMP3	Silencing of TIMPs, especially TIMP3, causes hyperactivity of ADAM10/17, leading to overproduction of TNFα, which in turn increased the expressions of DKK1, an inhibitor of WNT pathways. Overexpression of TIMP3 causes an inactivation of PI3K/AKT pathway, reducing proliferation and survival of osteosarcoma cells.	[49-50]
	-0.763570975	9.14E-07	0.00268453	PLAU	PLAU gene encodes urokinase plasminogen activator (uPAR) which affects bone homeostasis by regulating osteoblasts and osteoclasts. The knockout of uPAR caused a favorable osteoblast proliferation and a decrease in osteoclast number.	[51]
	-1.42031	4.07E-16	3.74E-12	ARC	ARC promotes BMSC proliferation and inhibits cell apoptosis	[52]
t= 3 days	5.03515	1.78E-03	1.75E-02	MMP10	MMP10 induces differentiation of myoblasts into osteoblasts. MMP10 deficiency cause chondrocyte hypertrophy and chondrocyte death via apoptosis. MMP10 knockdown decreased the gene and protein expressions of COL2, COL10, RUNX2 and MMP13 in chondrocytes, as well as significant increase in apoptosis.	[53]
	4.27743	1.29E-09	5.59E-08	ALK	ALK gene makes proteins called ALK receptor tyrosine kinases, which activate multiple pathways including PI3K/AKT/mTOR and MAPK.	[54]
	3.71702	5.11E-06	0.00012	PIK3C2G	Belongs to phosphoinositide 3-kinase (PI3K) family involved in cell proliferation, survival, migration, oncogenic transformation, and intracellular protein trafficking, and plays a role in diseases like type II diabetes.	[55]
	3.43454	2.87E-04	0.00394	FGF12	FGF12 regulates vascular smooth muscle cells, where FGF12 is highly expressed in normal VSMCs compared to VMSCs from injury or atherosclerosis. FGF12 inhibit cell proliferation through p53 pathway and induced phenotypic changes through p38 MAPK pathway.	[56-57]

	2.42307	1.67E-15	1.47E-13	KCP	A positive regulator of BMP pathways. Promotes osteoblast differentiation by BMP2.	[58]
	2.30488	0.00250	0.02308	LEF1	LEF1 is an important downstream gene of the wnt/beta-catenin signaling pathway. Overexpression of LEF1 promoted cell proliferation and survival under hypoxic and oxidative stress environment.	[59]
	2.20461	1.04E-48	5.41E-46	THBD	THBD promotes endothelial proliferation, migration, and tube formation in vitro and enhances angiogenesis.	[60]
	2.12215	2.03E-09	8.54E-08	HAS1	HAS1 encodes hyaluronan (HA); HA is produced during wound healing and tissue repair to provide a scaffold for angiogenesis.	[61]
	-2.47050	1.87E-21	2.77E-19	WNT2	WNT2 is up-regulated throughout the differentiation period of BMSCs, along with WNT3A.	[62]
	-2.83869	4.96E-06	0.00012	CPZ	CPZ is secreted into ECM and directly binds to WNT-4, enhancing the Wnt-4 activity to promote WNT signaling and chondrocyte differentiation.	[63]
	-4.47356	1.15E-05	0.00024	C6	Involved in complement activation; C6 is part of a membrane attack complex that can insert into cell membrane and cause cells to lyse.	[64-65]
t= 7 days	3.54998	9.89E-05	0.00247	ELMOD1	ELMO1 positively regulates bone resorption in osteoclasts by promoting osteoclast differentiation with higher expressions of TRAP, NFATc1, and DC-STAMP. ELMO1 mediates RANKL-induced osteoclast differentiation via Rac1, p38, JNK, and AKT pathways.	[66]
	3.26720	0.00065	0.01158	BLID	Tumor suppressor; BLID is an apoptotic member of the Bcl-2 family.	[67]
	3.19984	0.00090	0.01483	HBD	HBD stands for hemoglobin subunit delta. Two alpha chains and two delta chains comprise 1-3% of adult hemoglobin.	[68]
	3.00207	0.00251	0.03224	CASC19	Cancer Susceptibility 19 gene is associated with proliferation, inhibition of apoptosis, and metastasis of many cancers including colorectal cancer, gliomas, and gastric cancers.	[69-71]
	2.56827	0.00083	0.01397	KLHL38	Promotes proliferation of cancer cells by increasing cyclindD1, cyclin B, and c-myc and downregulation of p21. Also enhances migration and invasion of cancer by up-regulating RhoA and MMP-9 and down-regulating E-cadherin. Also known to activate Akt pathway.	[72]
	-2.01366	0.00267	0.03413	ZC3H11A	Loss of ZC3H11A enhances NF-kB signaling pathway, up-regulation of genes related to innate immunity, such as IL-6.	[73]
	-2.02179	0.00339	0.04002	ROBO2	Expressed in osteoblasts; binding of Slit3 to Robo2 activates β-catenin and promotes new bone formation.	[74]
	-2.20103	0.00292	0.03645	ARHGEF16	Involved in protein-protein or protein-lipid interactions. ARHGEF16 binds to ELMO1 and promotes the clearing of apoptotic cells via RhoG-dependent Rac1 activation.	[75]
	-2.43843	1.33E-12	1.75E-10	COMP	ECM protein is dominantly found in cartilage; COMP promotes BMP-2-dependent osteogenesis.	[76]

	-2.48456	6.56E-05	0.00172	ADRA2A	Only present in osteoblasts and bone-lining cells and not in osteocytes because they have the ADRA2A receptors; involved in bone turnover and remodeling. [77]
	-2.53895	0.00065	0.01165	DIRAS3	Regulates autophagy; Inhibits PI3K/AKT, JAK/STAT, RAS/MAPK to prevent cancer cell growth, migration, and angiogenesis. Also promotes ROS-mediated apoptosis with KRAS mutations. [78-79]
	-2.59298	0.00011	0.00264	MRPS30-DT	MRPS30 (mitochondrial ribosomal protein S30) help in protein synthesis in mitochondria. MRPS30-DT significantly promotes breast cancer cell proliferation, invasion, and metastasis, and inhibits tumor cell apoptosis. [80]
	-2.63431	6.03E-05	0.00160	SFRP2	Inhibits canonical Wnt signaling by phosphorylating and decreasing the expression of nuclear β-catenin. SFRP2 knockout in mice showed impaired bone regeneration and less trabecular bone. SFRP2-deficient in BMSCs decreased RUNX2 and Osx expression, as well as LRP6 and Wnt target genes like Axin2, c-myc, and Cyclin D1. [81-82]
	-3.22750	0.00126	0.01896	TNFSF18	Gene encodes a cytokine belonging to TNF ligand family and is expressed in endothelial cells; a strong negative regulator of osteoclastogenesis via inhibiting M-CSF-induced RANK expression. [83]
	-3.69445	0.00136	0.02014	HRH4	Histamine Receptor H4 plays a role in inflammation and allergies. Associated with inflammatory diseases like arthritis. [84]

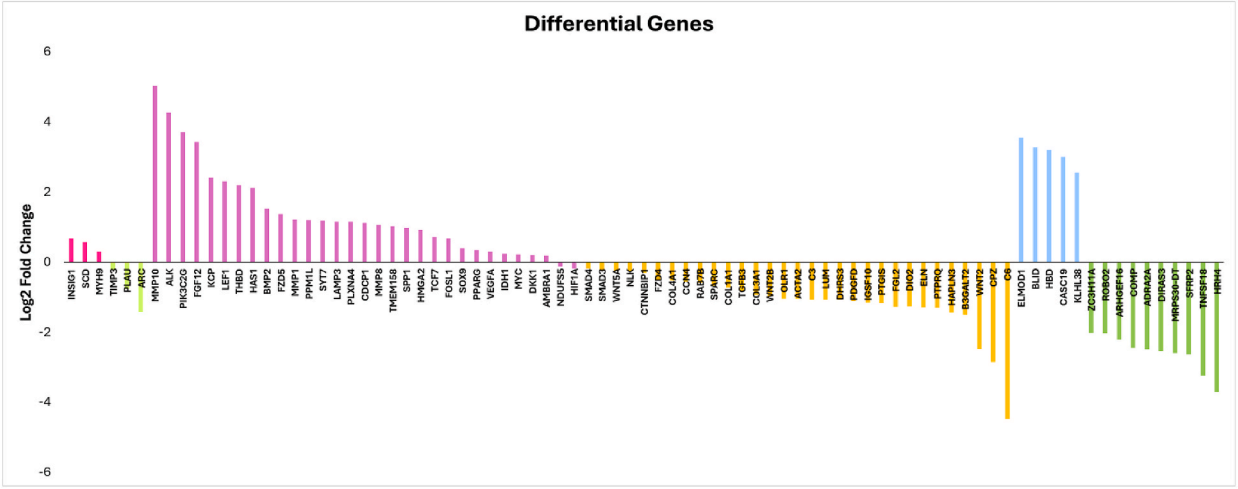

if Mg was affecting the endogenous production of ROS in mitochondria during oxidative phosphorylation. The fluorescence intensities were divided by that of the control group at t = 1 day, so relatively, mitochondrial ROS levels were generally higher for the 6-hr group. Relative to its control, cells treated with Mg 400 μg/mL showed a significant decrease in mitochondrial ROS at t = 6 h (Fig. 4G), but there were no changes by t = 1 day (Fig. 4H). So, the significant decrease in ROS we see at t = 1 day after Mg treatment is not due to mitochondria. We finally wanted to determine how Mg particles modulate the ROS levels in a simulated inflammatory environment (i.e., in the presence of H_2O_2). Hoechst measurements showed no changes after Mg particle treatment in different oxidative stress levels (Fig. 4I), which is different from Mg particle treatment in normal conditions (refer to Fig. 4B). Again, cell proliferation was found directly linked to total intracellular ROS levels because cells treated with Mg in simulated inflammatory conditions showed significantly higher ROS (around 0.9–1.1) compared to those treated with Mg in normal conditions (0.6–0.8) (Fig. 4J). In other words, Mg was able to decrease the total intracellular ROS that enhanced cell proliferation in normal conditions, but under oxidative stress, Mg did not reduce the intracellular ROS levels. We repeated the experiment with the addition of sodium pyruvate and this time, the Hoechst measurement showed a slight decrease in live cells for those treated with Mg at higher H_2O_2 of 8.8 ηM compared to 4.4 ηM, but the change was too slight (less than %5; Fig. 4K). The total ROS levels showed no changes except for the highest particle concentration of 400 μg/mL in a high oxidative stress environment (from 1 to about 0.75, about 25 % reduction; Fig. 4L).

In vivo ROS levels were also measured in Balb/c nude mice (Fig. 5). Different Mg sizes of either 1 mm or 2 mm rods were used to see if the size affected the ROS production (Fig. 5A). We implanted Mg rods subcutaneously with either PBS or 50 μM H_2O_2 solutions to mimic simulated inflammatory conditions. The 50 μM H_2O_2 concentration was chosen based on a study that reported that 50 μM H_2O_2 or higher levels are detected in plasma during inflammation [43]. We used two control groups, injecting either PBS or 50 μM H_2O_2 inside the subcutaneous pocket with or without Mg rods, which showed that no ROS signals were detected without Mg rods (Fig. 5C). When pure Mg rods were inserted into the pocket in either PBS or 50 μM H_2O_2, there were significant amounts of ROS detected after 1 h of surgery (Fig. 5D), up to 1 day, and then quickly reduced over time until no ROS was detected at 3 days. The area of red-yellow regions was quantified as % and graphed (Fig. 5B). There was no significant difference in the ROS signal due to Mg rod size. However, in PBS, the 2 mm Mg rod showed more positive ROS detection when the 1 mm Mg rod stopped showing any ROS signal at t = 1 day. 1 mm Mg rod in 50 μM H_2O_2 showed more ROS signals than 1 mm Mg rod in PBS at t = 1 day as well, so 50 μM H_2O_2 may help to excessively corrode Mg for a longer time. Although the variability was high, the *in vivo* ROS was detected at early time points when Mg rods were implanted.

Transcriptome sequencing of hBMSCs treated with Mg 100 μg/mL for different times showed that the PI3K/Akt pathway was enriched for all time points (Fig. 6). The PI3K/Akt/mTOR pathway regulates cell survival and proliferation, and this signaling pathway may be the major pathway affected by Mg that either inhibited or promoted cell

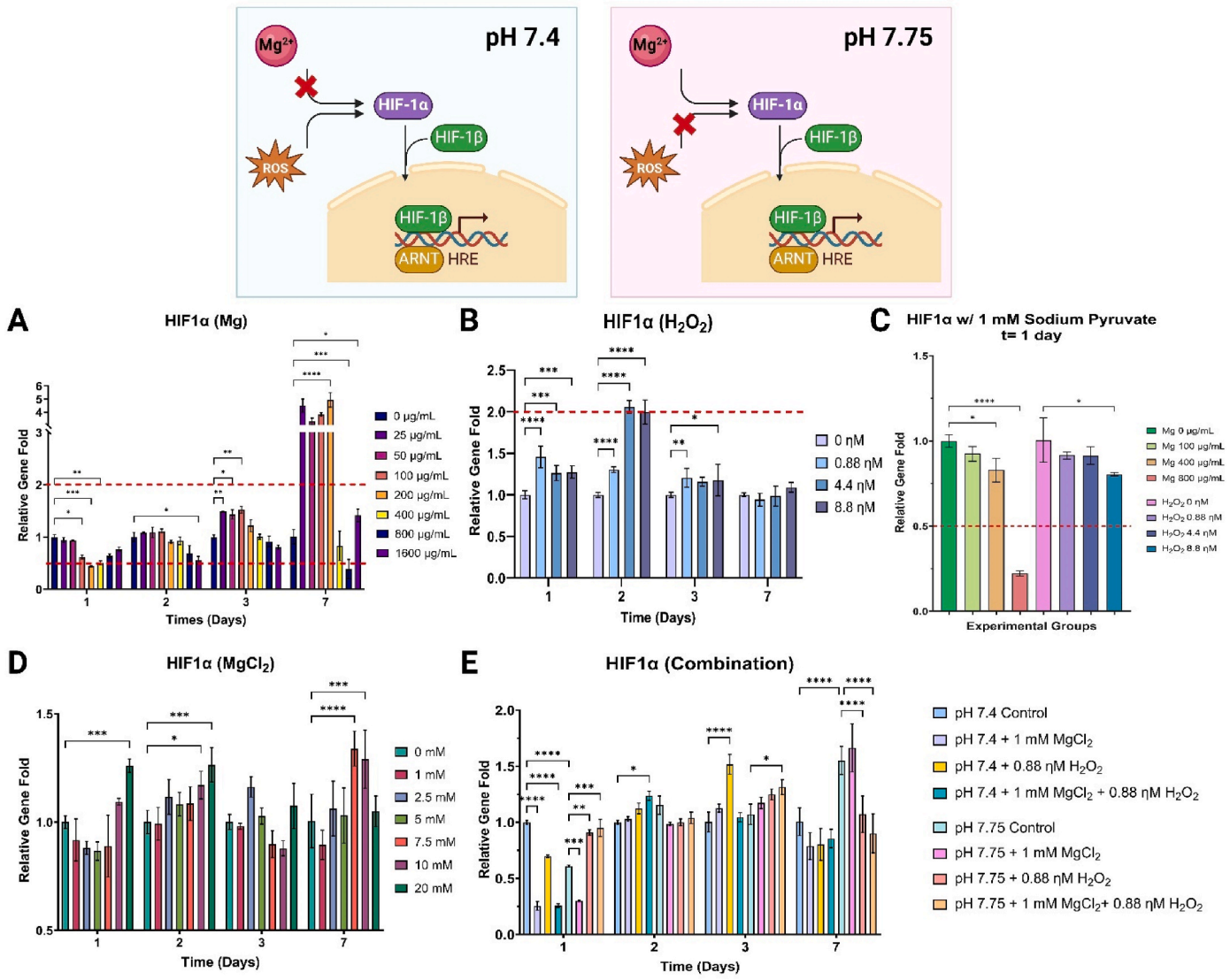

Fig. 8. HIF1α gene expressions for hBMSCs treated with A) Mg particles, B) H_2O_2, C) Mg or H_2O_2 with 1 mM sodium pyruvate, D) $MgCl_2$, and E) combinations of Mg ions and H_2O_2 in different pH levels (chronic). Two-way ANOVA analysis was used to find statistical significance using GraphPad Prism 10.2 software, where *p < 0.05, **p < 0.01, ***p < 0.001, and ****p < 0.0001.

proliferation over time (refer to Fig. 2). Other enriched pathways based on KEGG analysis included ECM-receptor interactions, chemical carcinogenesis-reactive oxygen species, AGE-RAGE pathway, cell cycle, and citrate cycle, which were also found significant in proteome analysis (Fig. 7). Mitophagy, oxidative phosphorylation, and metabolic pathways were enriched as well, indicating that mitochondria and metabolism are also significantly affected by Mg. GO enrichment pathways were similar, showing significance in osteoblast differentiation, cell migration, collagen metabolism and homeostasis, ossification, and so on. The differential genes that showed a higher log2fold change greater than ±2-fold are listed in Table 3. Differential genes with log2 fold change higher than 2 were listed with their p-values lower than 0.05, and many of them were involved in proliferation and cell survival, osteogenesis, angiogenesis, and mitochondrial functions/homeostasis (Fig. 8). Based on the transcriptome sequencing data and proteome analysis, HIF1α gene was one of the key genes found significant in many enrichment pathways of Mg, including PI3K/Akt, chemical carcinogenesis- ROS, cell cycle, and WNT. HIF1α was consistently found down-regulated during early corrosion of Mg: −0.186 log2fold change with a p-value of 5.21E-9 at t = 3 days based on transcriptome sequencing and −0.5 log2fold change with a p-value of 2.58E-5 at t = 2 days via proteome analysis. The early down-regulation of HIF1α was confirmed by qPCR, where HIF1α expression was reduced by almost half at the same particle concentration of 100 μg/mL at t = 1 day (Fig. 8). KEGG and GO pathways for other particle concentrations, as well as differential genes found significant are listed in SFigs. 10 and 11.

HIF1α gene expressions were measured in different experimental conditions to see which factors from oxidation and reduction reactions dominantly affect HIF1α (Fig. 8). For Mg particles, HIF1α decreased significantly for intermediate particle concentrations between 200 and 400 μg/mL at t = 1 day (Fig. 8A). However, eventually the lower concentrations of Mg between 25 and 200 μg/mL began to up-regulate HIF1α with a 4-5-fold increase at t = 7 days. This is interesting since these were also the concentrations that showed higher cell proliferation at t = 7 days (refer to Fig. 2E). On the other hand, the high concentrations between 400 and 1600 μg/mL did not up-regulate HIF1α, and these were the concentrations that showed a significant drop in viability compared to the control group (Fig. 8A). HIF1α is closely related to oxidative stress and hypoxia, and so, cells were treated with H_2O_2 to measure the changes in HIF1α expressions (Fig. 8B). H_2O_2 up-regulated HIF1α in the first 3 days, especially on day 2 for the higher concentrations groups of 4.4–8.8 ηM, resulting in over 2-fold change. Cells were

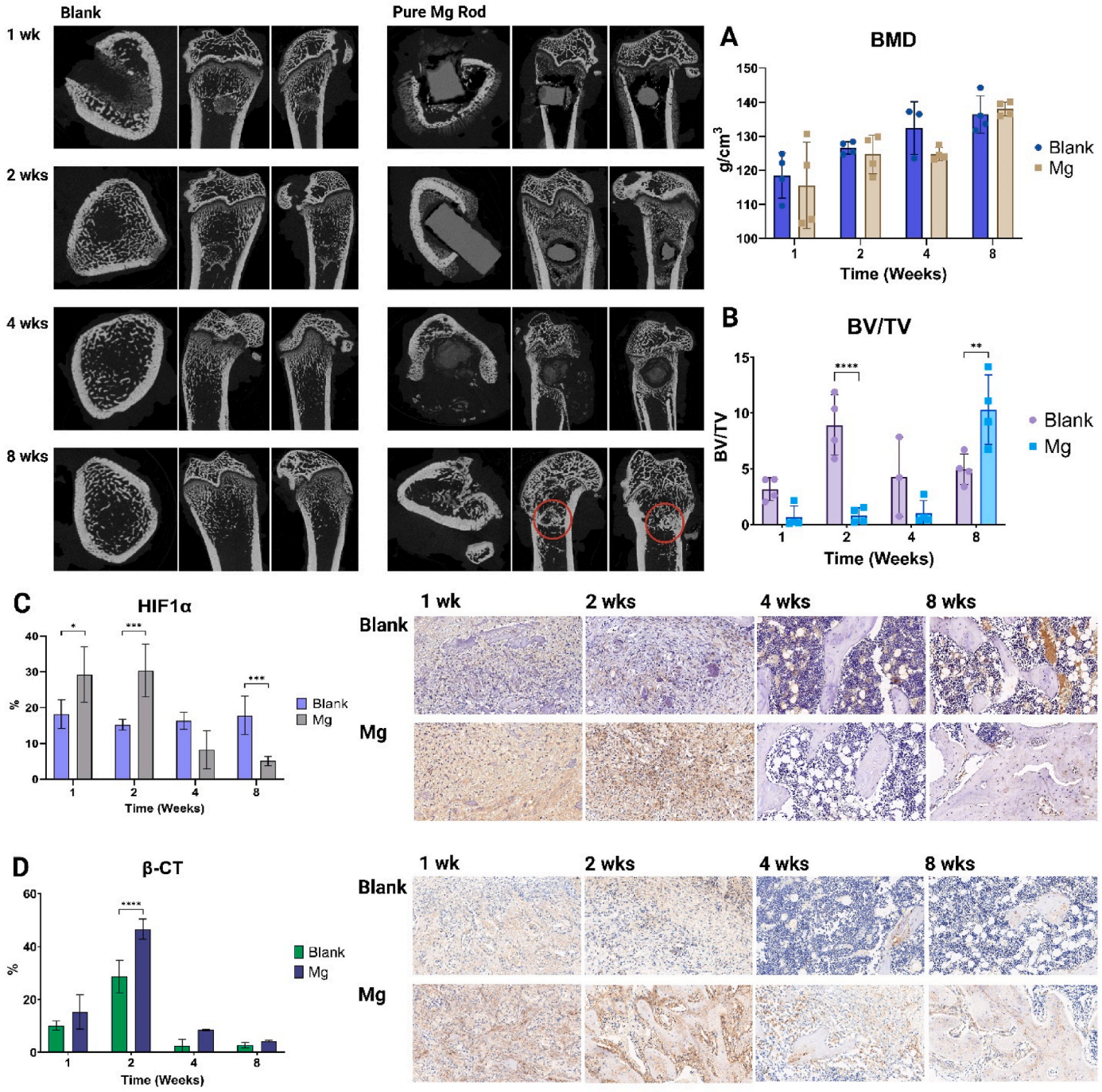

Fig. 9. *In vivo* bone defect femur analysis. Bone was drilled in 2 mm size and either pure Mg rod (d = 2 mm x h = 5 mm) was implanted or left blank. BMD and BV/TV were analyzed from the micro-CT. IHC staining was done to measure HIF1α and β-catenin expressions in tissues, which was analyzed using Image J and IHC Toolbox (https://imagej.net/ij/plugins/ihc-toolbox/). Two-way ANOVA analysis was used to find statistical significance using GraphPad Prism 10.2 software, where *p < 0.05, **p < 0.01, ***p < 0.001, and ****p < 0.0001.

treated with either Mg or H_2O_2 in 1 mM sodium pyruvate, and for H_2O_2, HIF1α was down-regulated instead of up-regulated. For Mg, HIF1α was already down-regulated at t = 1 day and remained down-regulated with sodium pyruvate (Fig. 8C). Although HIF1α was far more down-regulated for the 400 μg/mL group without sodium pyruvate at 0.5-fold compared to those with sodium pyruvate at 0.8-fold, this variability could just be due to technical variability and particle distribution. The fact that the addition of sodium pyruvate in the H_2O_2 experiment prevented the increase in HIF1α expression revealed that H_2O_2 is the source. However, since Mg, in general, decreased HIF1α expressions at t = 1 day regardless of sodium pyruvate meant that H_2O_2 is not the major factor affecting HIF1α. Other ROS could be involved, or H_2O_2 in conjunction with other factors could be affecting HIF1α together. For example, cells treated with Mg ions and H_2O_2 at pH of 7.4 showed a significant down-regulation of HIF1α compared to those treated with H_2O_2 at pH of 7.4 alone (Fig. 8E). Since the actual *in vitro* pH of Mg particles by t = 1 day is not alkaline (see SFig. 7), perhaps Mg ions and H_2O_2 may be needed together. HIF1α expressions were also measured after $MgCl_2$ treatment, which significantly increased HIF1α for the higher dosages between 7.5 and 20 mM, although the change was less

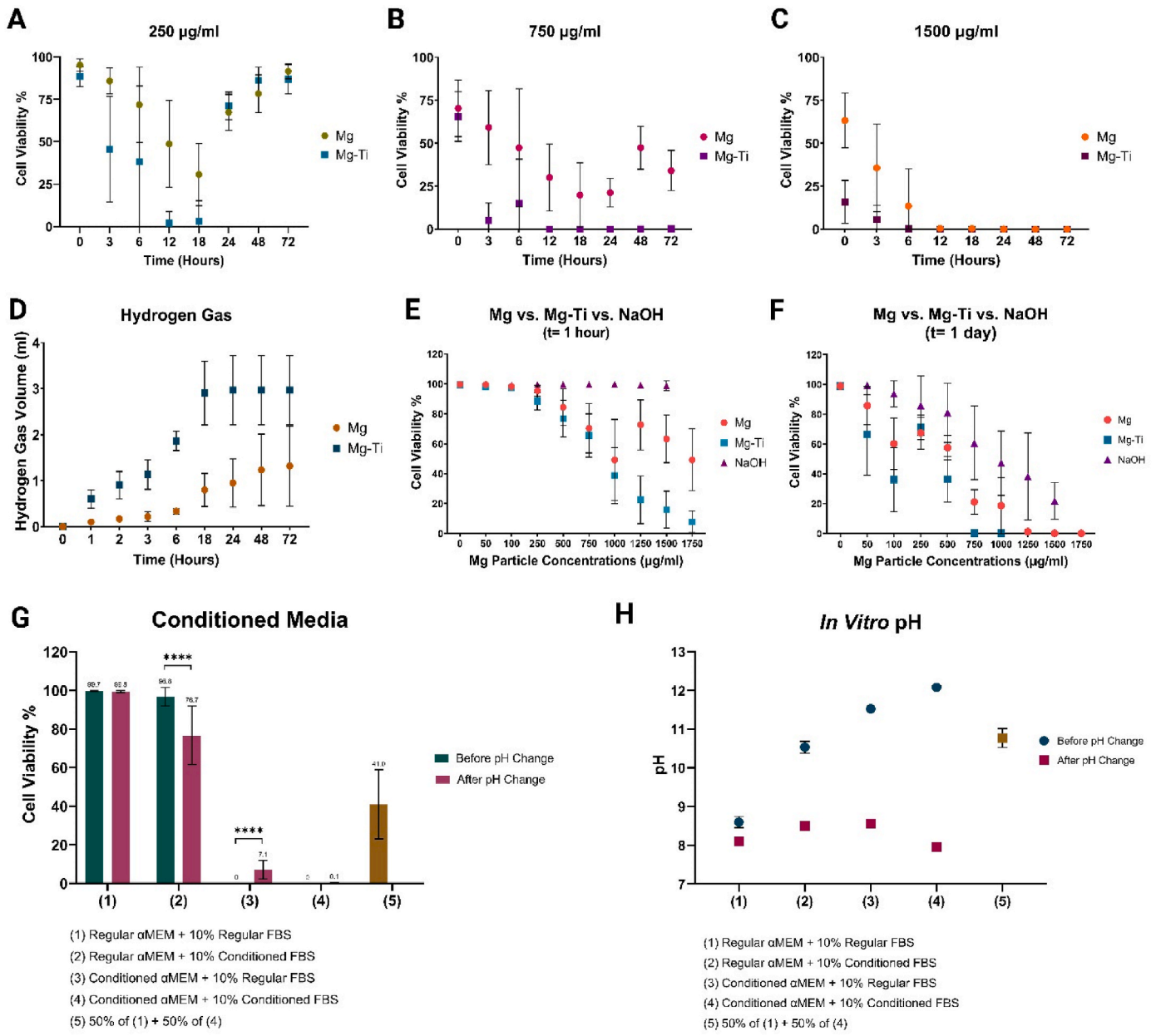

Fig. 10. MC3T3-E1 cell viability after Mg or Mg-Ti treatment of A) 250, B) 750, and C) 1500 μg/mL from t = 0–72 h. D) Hydrogen gas volume measured during corrosion of 0.05 g of Mg or Mg-Ti in 5 mL pipette with funnel in a 30 mL complete media solution. MC3T3-E1 cell viability after treating cells with different concentrations of Mg, Mg-Ti (0–1750 μg/mL), or NaOH that resulted in alkaline pH between 7 and 11 for E) t = 1 h and F) t = 1 day. G) MC3T3-E1 cell viability after treating cells in different conditioned media groups before and after adjusting pH using HCl, and H) actual *in vitro* pH before and after adjustment.

than 1.5-fold (Fig. 8D). The combination experiment could not precisely replicate Mg corrosion, but measurement of HIF1α in different combinations still provided some knowledge (Fig. 8E). One of the interesting observations was that all groups that contained Mg ions showed a significant down-regulation of HIF1α at t = 1 day, regardless of pH. Please note that this experiment is different from the $MgCl_2$ experiment in that the media was adjusted using either HCl or NaOH to specifically adjust the pH to either 7.4 or 7.75 at t = 0 h, and this media refreshed every 12 h. In fact, the pH 7.4 + 1 mM $MgCl_2$ group has been given this media twice by t = 1 day (once at t = 0 h and another at t = 12 h) and 14 times by t = 7 days. This study shows that HCl and NaOH with Mg ions have an adverse effect on HIF1α at t = 1 day, although the mechanism is unclear. At t = 3 days, there is a significant up-regulation of HIF1α when cells are treated with only H_2O_2 at a pH 7.4 (about a 1.5-fold increase) and when cells are treated with $MgCl_2$ and H_2O_2 at a pH 7.75 (about a 1.2-fold increase). Over time, at t = 7 days, only those cultured in chronic alkaline pH or those treated with Mg ions in chronic alkaline pH significantly increased HIF1α (about a 1.5-fold increase). For simplicity, it seems that Mg ions do not up-regulate HIF1α at a pH of 7.4 at all times, while H_2O_2 does not up-regulate HIF1α too well at alkaline pH at all times, summarized in schematic illustrations above the graphs. Overall, none of the experiments could increase HIF1α expressions like Mg particles, and HIF1α is one of the key genes responsible for enhanced proliferation seen in t = 7 days.

Next, we did an *in vivo* investigation of large femur defects and implantation of pure Mg rods to measure new bone formation and the changes in HIF1α and β-catenin expressions to understand HIF1α and β-catenin relationships in the WNT pathway. A large defect was made in the rat femur (2 mm in size), and either a pure Mg rod was inserted or left blank. The rats were sacrificed at different time points, 1, 2, 4, and 8

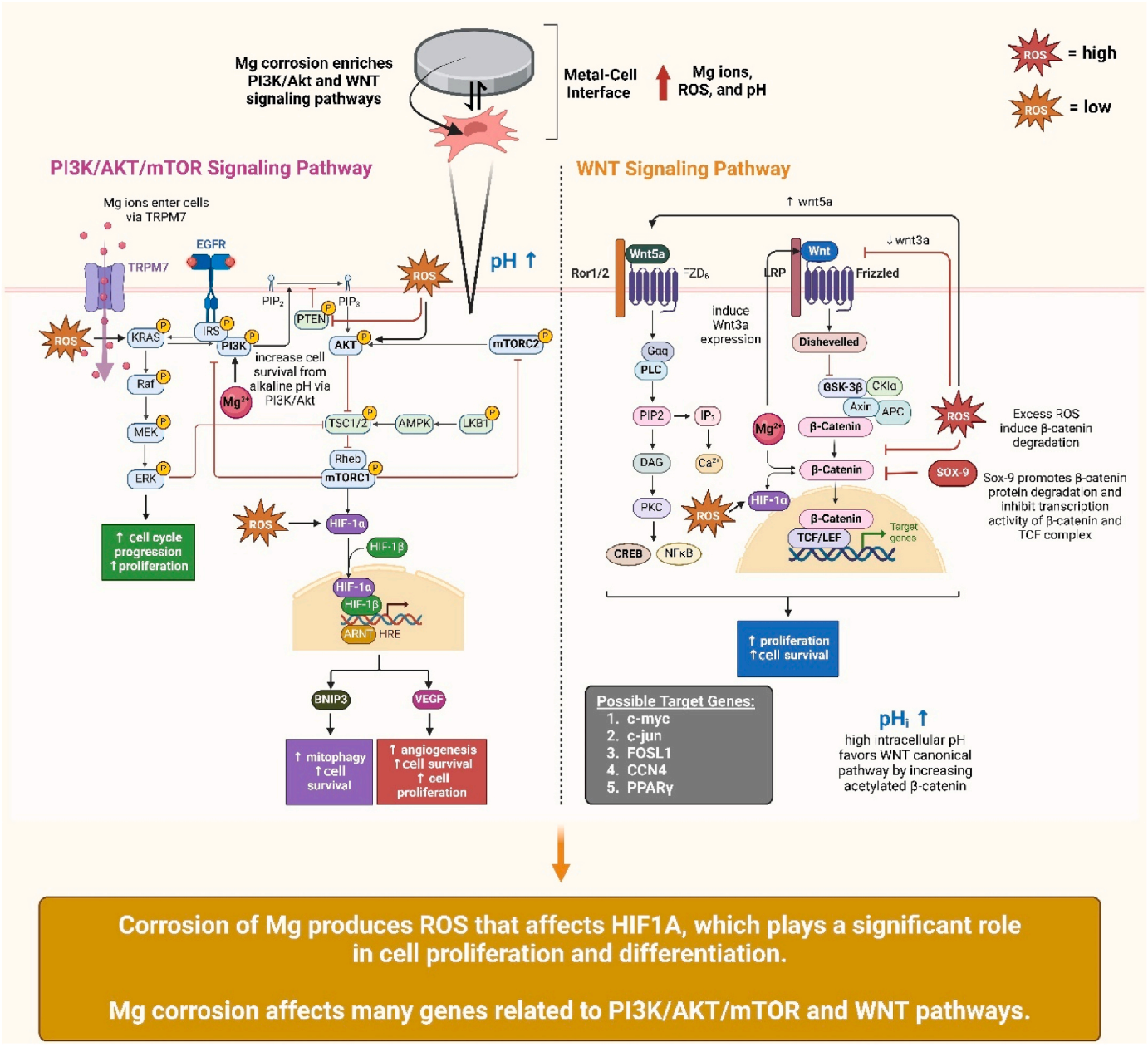

Fig. 11. Schematic illustrations show major signaling pathways affected by Mg corrosion, confirmed with transcriptome sequencing, proteome analysis, and qPCR, as well as supported by other references to encapsulate how reduction reactions affect the following pathways [101–105].

weeks, to see the changes in bone mineral density (BMD, g/cm^3) and bone volume/total volume (BV/TV, %). The region of interest was chosen as a circle, including the areas of the Mg implant rod and about 3 mm around the implant. Based on the micro-CT analysis, there were no significant changes in BMD between blank and pure Mg groups, indicating that pure Mg itself did not increase the local bone mineral density in rats that are otherwise healthy besides the large defect surgically drilled for the purpose of the experiment (Fig. 9A). However, there were significant changes in BV/TV, where initially in the first 2 weeks, the blank group showed some formation of bone, which then started to decrease over time at 4–8 weeks (Fig. 9B). Although the data is not shown here, TRAP staining showed that the increase in TRAP activity around this time probably increased osteoclast activity, initiating bone resorption and reducing new bone formation (this data is to be published elsewhere). On the other hand, pure Mg showed low BV/TV in the first 4 weeks as pure Mg was actively corroding, even killing nearby healthy bone (creating a gap between the implant and surrounding tissues) (Fig. 9B). However, as Mg degraded almost completely, new bones began to form in the areas that used to be occupied by the Mg implant, indicated by red circles (Fig. 9B). The average BV/TV was double that of the blank group (about 5 % for blank groups; about 10 % for Mg groups) at 8 weeks of implantation. Furthermore, immunohistochemistry (IHC) staining of HIF1α showed that HIF1α expressions were higher for pure Mg in the first 2 weeks, which were then significantly reduced at 4 and 8 weeks (Fig. 9C). Interestingly, IHC of β-catenin was also increased when HIF1α was increased in the first 2 weeks and down-regulated with HIF1α at 4 and 8 weeks, showing a clear relationship between them.

We also briefly investigated the cytotoxic response of Mg and Mg-Ti by measuring MC3T3-E1 viability over time for different particle concentrations to show that alkaline pH is not the dominating factor that induces *in vitro* cytotoxicity. Cell viability was measured for different particle concentrations of Mg and Mg-Ti over time, and the cell viability was drastically different per concentration group. For instance, Mg and Mg-Ti 250 μg/mL showed a significant decrease in cell viability that

reduced the overall cell population down to almost 5 %; however, these remaining cells were able to proliferate and recover the cell viability afterward (Fig. 10A). For higher concentrations of 750 μg/mL, cell viability dropped down to 0 for Mg-Ti, while for Mg, about 75 % cells were killed (Fig. 10B). More cells survived for the 750 μg/mL group than 250 μg/mL group, and yet, 25 % of the live cells couldn't proliferate as if they are under cell cycle arrest. At high concentrations of 1500 μg/mL, Mg and Mg-Ti both exponentially killed cells over time, except Mg-Ti killed slightly faster (Fig. 10C). The reason for the higher cytotoxicity of Mg-Ti is due to the higher corrosion rate, which was proven by measuring hydrogen gas directly proportional to the corrosion rate (Fig. 10D). Mg-Ti produces about 3 times more hydrogen gas volume than Mg. So, we can conclude that Mg-Ti corrodes about 3 times faster than pure Mg. In order to understand if Mg-Ti is killing faster due to higher alkaline pH, cell viability of Mg and Mg-Ti were compared with those treated with different pH levels adjusted using NaOH. The data shows that while high alkaline pH is also detrimental to cell viability, alkaline pH kills slowly. At t = 1 h, Mg and Mg-Ti already killed cell viability proportional to the particle concentrations; however, alkaline pH did not have any effect, even for those treated at a pH of 11 (Fig. 10E). Only after t = 1 day, NaOH also began to kill cells, which was also proportional to the degree of alkalinity (Fig. 10F). Based on these data, we can make several assumptions. First, cell proliferation, cell cycle arrest, and cytotoxicity dependent on particle concentrations were similar to how ROS affected cells, according to Martin et al. [85]. Second, alkaline pH alone cannot kill cells quickly and does not explain the higher cytotoxicity of Mg-Ti since the pH of Mg and Mg-Ti did not show any statistical difference [86]. Since we have already evidenced that ROS levels increase during Mg corrosion, we can safely conclude that cytotoxicity is due to high ROS production and accumulation. Finally, the conditioned media significantly reduced the viability, although no particles were actively corroding in the presence of Mg particles (Fig. 10G). Adjusting the pH using HCl (Fig. 10H) did not increase the cell viability, further supporting the idea that pH is not the sole cause of cytotoxicity. SFig. 12 shows that the media is altered, changing the opacity of the solution, further supported by FTIR and XRD analysis. It seems that ROS aggregates the proteins and other biomolecules essential for cell nutrients and growth, resulting in a decrease in viability rather than solely due to the changes in the pH. However, further investigations of protein analysis are required.

4. Discussion

This study provides a fundamental basis and some novel insights into the importance of reduction reactions. First, Mg corrosion is not just about metal oxidation, and we cannot assume that Mg alloys are biocompatible solely because Mg ions are essential trace elements. While Mg alloys may be designed to increase corrosion resistance, Mg alloys still degrade at some rate, so we need to study how the reduction reactions at different rates affect the local microenvironment and nearby cells. Also, we need to consider how these by-products simultaneously regulate cells, which may be different than how they affect cells independently. For example, Mg ions may affect cells differently at alkaline or acidic pH compared to physiological pH, as well as under hypoxic or high oxidative stress conditions. For all our *in vitro* studies, we directly cultured Mg particles with cells in a concentration-dependent manner to study a range that would not induce too much cytotoxicity and observe other biological events that occur at low-moderate particle concentrations (i.e., low-moderate corrosion rates). We did not use the preconditioned media method suggested by ISO 10993:5 because this eliminates the direct interactions between biomaterials and cells and the exposure of cells to intermediate species produced during Mg corrosion, like ROS.

There are some important points that need to be emphasized based on this study. Mg reduced total intracellular ROS in normal, non-oxidative conditions, which enhanced cell proliferation. PI3K/Akt/mTOR pathway was enriched for the Mg groups at all times, involved in regulating cell proliferation and differentiation, and HIF1α is a downstream gene that is activated by this pathway [87]. HIF1α is also known to protect cells from ROS-induced apoptosis by translocating into the mitochondria in response to oxidative stress, and one mechanism is by increasing mitophagy via HIF1α/BNIP-3 axis [88,89]. We found that Mg significantly down-regulates HIF1α early during active corrosion, resulting in the down-regulation of BNIP-3 by −1.5-fold. In addition, oxidative phosphorylation was also down-regulated at early time points by decreasing the expressions of genes/proteins that make up the components of complexes I-IV, and by doing so, reducing oxidative phosphorylation. This may explain why we saw a slight decrease in mitochondrial ROS at t = 6 h. Furthermore, AMBRA1 that also regulates mitophagy was up-regulated by 0.5-fold change, which is known to negatively regulate ALDH1B1, a member of aldehyde dehydrogenase (ALDH) family of $NAD(P)^+$-dependent enzymes, and ALDH1B1 has been found to directly mediate HIF1α and β-catenin [90]. Overexpression of AMBRA1 causes the down-regulation of ALDH1B1 and subsequent down-regulation of WNT/β-catenin, PI3K/Akt, and TGF-β pathways [90]. PI3K/Akt is also involved in positively regulating HIF1α via mTOR, and HIF1α regulates glucose metabolism by switching from oxidative phosphorylation to glycolysis [87]. In addition, there is a close relationship and interactions between HIF1α and β-catenin. First, β-catenin accumulation is known to activate PI3K/Akt, which then positively regulates HIF1α to enhance cell survival and proliferation [91]. However, HIF1α stabilized in hypoxia or oxidative stress can also inactivate β-catenin, causing a cell growth arrest [92]. This biphasic effect seems to depend on the ROS levels, not Mg ions.

In vivo studies further support the close relationship between HIF1α and β-catenin, regulated during Mg corrosion. *In vivo* studies showed that HIF1α and β-catenin were up-regulated in the first 2 weeks and then reduced at 4 and 8 weeks, indicating that they are critical upstream genes that need to be activated for osteogenesis and new bone formation. So, in this study, we show that Mg activation of PI3K/Akt/mTOR and downstream gene HIF1α due to changes in ROS also contributes to the promotion of canonical WNT/β-catenin pathway, critical for osteogenesis, in addition to the conventional concept that Mg ions are primarily responsible for bone formation. Furthermore, we show that cytotoxicity due to galvanic coupling of Mg and Ti is not due to alkaline pH since Mg and Mg-Ti kill cells within 1 h, as opposed to slow killing of alkaline pH only after 1 day. The killing is proportional to concentrations, where the intermediate range induces cycle arrest and high dosage induces cell death, and this pattern is the same when cells are treated with different concentrations of ROS [93]. So, Mg alloys can kill unwanted cells quickly independent from alkaline pH, typically considered a major contributor to Mg cytotoxicity. Since ROS has a proximal effect, Mg-Ti can be a promising therapeutic agent that can kill local tumors and bacterial infections without causing adverse effects on healthy tissues. Hydrogen gas is also produced as a by-product of reduction reactions, which was neglected for having an effect on *in vitro* cytotoxicity because hydrogen gas is insoluble in water. Hydrogen gas does not readily dissolve in most solutions, including cell culture media, but floats on top of the solution as bubbles and even dissipates into the atmosphere, having a minimal effect. So, *in vitro* cytotoxicity of Mg in our study was primarily due to ROS and alkaline pH. However, *in vitro* and *in vivo* cytotoxicity is different, where hydrogen gas has more significance *in vivo*, as quick and large accumulations of hydrogen gas pockets have been found to cause tissue necrosis if not adequately punctured [94,95], and hydrogen gas when produced at a proper rate is an antioxidant and scavenge ROS [96]. Therefore, for future studies, it will be interesting to study more closely how the ROS and hydrogen gas produced from the Mg surface during degradation simultaneously affect the microenvironment and cells temporally and spatially. Based on this study, we should carefully consider the reduction reactions affecting biology when designing metal-based biomaterials, especially in pathological conditions with highly skewed microenvironments regarding environmental

pH, oxidative stress, hypoxia, and inflammation. We need to understand that Mg alloys have double-edged effects that can either yield beneficial effects to resolve inflammation and promote tissue regeneration but can also cause harmful effects that can kill cells, and the corrosion behavior depends not only on the material itself but also on the surrounding microenvironment and cells. In addition, the biological-biochemical effects ROS have on cells and microenvironments vary across different cell types and conditions. Not all cells respond the same to ROS, where certain cells have higher resistance and plasticity against oxidative stress, such as cancer cells [97] and macrophages [98]. The relationship between ROS and macrophages was determined by exposing macrophages to increasing amounts of hydrogen peroxide for over a month up to a sub-lethal amount and found that macrophages became resistant to chronic exposure to oxidative stress and adapted to high ROS environment by increasing the catalase expression by over 30-fold [98]. On the other hand, T cells under the same experimental condition could not adapt to the increasing dosage of ROS; however, when T cells were cultured in the conditioned media of "adapted" macrophages (i.e., those that survived the high ROS), T cells also survived better at high ROS levels, indicating that some macrophage-secreted cytokines or chemokines protected T cells from oxidative stress [98]. Macrophages have self-protection against oxidative stress via Mst1/2, which regulates the antioxidant transcription of Nrf2 [99]. Also, ROS levels are highly skewed in aging due to the contributions of multiple hallmarks of aging, such as mitochondrial dysfunction, chronic inflammation, and so forth [100]. Therefore, we should recognize the importance of reduction reactions and how they contribute to and alter the microenvironment and regulate cell functions in aging and diseases. In summary, we show that reduction reactions significantly affect cell behaviors depending on the corrosion rate. Fig. 11 shows an overall summary of the key pathways affected by Mg corrosion.

5. Conclusion and future perspectives

In conclusion, reduction reactions are perhaps more critical since they induce different biological responses depending on their rate and duration, from cell proliferation/survival to cell growth arrest and death. Mg alloys hold great promise in targeted therapy as reduction reactions that produce ROS can be used to locally target and kill cancers and unwanted cells while minimizing damage to healthy tissues. Furthermore, we found that reduction reactions equally contribute to cell survival/proliferation and osteogenesis due to alkaline pH and ROS produced as by-products. ROS is closely associated with HIF1α, and Mg corrosion has been found to regulate the PI3K/Akt/mTOR pathway and other pathways that modulate mitochondrial functions like mitophagy and oxidative phosphorylation. While this study was generally broad, further research is desired to understand how metal corrosion can control and regulate certain biological processes found here. In addition, an in-depth investigation of hydrogen gas is desired, especially when they are produced together with ROS during Mg corrosion. While we studied Mg alloys, all metals that corrode accompany reduction reactions, so our concept can be expanded and adapted to other metals. In the future, we should study promising Mg alloys in diseased and aged microenvironments and how reduction reactions can be used for targeted therapy.

CRediT authorship contribution statement

Jua Kim: Writing – review & editing, Writing – original draft, Visualization, Validation, Project administration, Methodology, Investigation, Funding acquisition, Formal analysis, Data curation, Conceptualization. **Jeremy L. Gilbert:** Supervision, Funding acquisition. **William W. Lv:** Funding acquisition. **Ping Du:** Supervision, Funding acquisition. **Haobo Pan:** Supervision, Funding acquisition, Conceptualization.

Ethics approval and consent to participate

The animal experiments of this study were carried out based on the National Key R&D Program of China (approval No. 2021YFC2400500 and IACUC No. SIAT-IACUC-20230216-YYS-TXXZX-PHB-A2149-01). All animal experiments in this study were consented and supervised by the Animal Research Committees of Shenzhen Institute of Advanced Technology, Chinese Academy of Science. All animal experiments complied with the ARRIVE guidelines and were carried out in accordance with the U.K. Animals (Scientific Procedures) Act 1986 and associated guidelines.

Data availability statement

The data that support the findings of this study are available on reasonable requests from the corresponding authors.

Declaration of competing interest

The authors declare the following personal relationships which may be considered as potential competing interests: Haobo Pan is currently employed by Shenzhen Healthemes Biotechnology Co. Ltd. Haobo Pan is an editorial board member for Bioactive Materials and was not involved in the editorial review or the decision to publish this article.

Acknowledgements

This work was supported by the National Key R&D Program of China (2021YFC2400500); Guangdong Marine Economic Development Program (GDNRC[2023]35); National Natural Science Foundation of China (U2001221, 32161160327, and 52250410340); NSFC-RGC Joint Research Scheme (N_HKU753121); the Shenzhen Science and Technology Program (JSGGKQTD20210831174330015, JCYJ20220531095811027); Shenzhen Medical Research Fund (B2302031).

Appendix A. Supplementary data

Supplementary data to this article can be found online at https://doi.org/10.1016/j.bioactmat.2024.11.020.

References

[1] C. Montoya, Y. Du, A.L. Gianforcaro, S. Orrego, M. Yang, P.I. Lelkes, On the road to smart biomaterials for bone research: definitions, concepts, advances, and outlook, Bone Res 9 (2021) 12, https://doi.org/10.1038/s41413-020-00131-z.

[2] Global metal implants and medical alloys market size, share, growth analysis, by material type (titanium and titanium alloys, stainless steel), by product type (orthopedic implants, dental implants), by application (Joint replacement, trauma and orthopedic surgeries) - industry forecast 2023-2030, Skyquest (2024). https://www.skyquestt.com/report/metal-implants-and-medical-alloys-market#:~:text=What. (Accessed 15 March 2024). %20is%20the%20global%20market,period%20(2023%2D2030).

[3] J.L. Gilbert, S. Sivan, Y. Liu, S.B. Kocagöz, C.M. Arnholt, S.M. Kurtz, Direct *in vivo* inflammatory cell-induced corrosion of CoCrMo alloy orthopedic implant surfaces, Biomed Mater Res A 103 (2015) 211–223, https://doi.org/10.1002/jbm.a.35165.

[4] H. Lee, M.A. Kurtz, J.L. Gilbert, Reactive oxygen species, electrode potential and pH affect CoCrMo alloy corrosion and semiconducting behavior in simulated inflammatory environments, Acta Biomater. (2024), https://doi.org/10.1016/j.actbio.2024.08.010.

[5] M.A. Kurtz, P. Khullar, J.L. Gilbert, Cathodic activation and inflammatory species are critical to simulating *in vivo* Ti-6Al-4V selective dissolution, Acta Biomater. 149 (2022) 399–409, https://doi.org/10.1016/j.actbio.2022.07.020.

[6] A. Manda-Handzlik, U. Demkow, Neutrophils: the role of oxidative and nitrosative stress in health and disease, in: M. Pokorski (Ed.), Pulmonary Infection, Advanced in Experimental Medicine and Biology, vol. 857, Springer, Cham, 2015, https://doi.org/10.1007/5584_2015_117.

[7] Z. Sheikh, P.J. Brooks, O. Barzilay, N. Fine, M. Glogauer, Macrophages, foreign body giant cells and their response to implantable biomaterials, Materials 8 (2015) 5671–5701, https://doi.org/10.3390/ma8095269.

[8] J.L. Gilbert, 2.4.3- metallic degradation and the biological environment, in: W. R. Wagner, G. Zhang, S.E. Sakiyama-Elbert, M.J. Yaszemski (Eds.), Biomaterials

Science, fourth ed., Academic Press, London, 2020, pp. 941–954, https://doi.org/10.1016/B978-0-12-816137-1.00063-5.
[9] M. He, L. Chen, M. Yin, S. Xu, Z. Liang, Review on magnesium and magnesium-based alloys as biomaterials for bone immobilization, J. Mater. Res. Technol. 23 (2023) 4396–4419, https://doi.org/10.1016/j.jmrt.2023.02.037.
[10] J. Kim, H. Pan, Effects of magnesium alloy corrosion on biological response-perspectives of metal-cell interaction, Prog. Mater. Sci. 133 (2023) 101039, https://doi.org/10.1016/j.pmatsci.2022.101039.
[11] G. Song, A. Atrens, D. St John, X. Wu, J. Nairn, The anodic dissolution of magnesium in chloride and sulphate solutions, Corrosion Sci. 39 (1997) 1981–2004, https://doi.org/10.1016/S0010-938X(97)00090-5.
[12] G. Morrison, Chapter 197 serum chloride, in: H.K. Walker, W.D. Hall, J.W. Hurs (Eds.), Clinical Methods: the History, Physical, and Laboratory Examinations, third ed., Butterworths, Boston, 1990. https://www.ncbi.nlm.nih.gov/books/NBK309/.
[13] M. Soltani, M. Souri, F. Moradi Kashkooli, Effects of hypoxia and nanocarrier size on pH-responsive nano-delivery system to solid tumors, Sci. Rep. 11 (2021) 19350, https://doi.org/10.1038/s41598-021-98638-w.
[14] T. Cui, et al., Micro-gel ensembles for accelerated healing of chronic wound via pH regulation, Adv. Sci. 9 (2022) 2201254, https://doi.org/10.1002/advs.202201254.
[15] M.A. Kurtz, P. Khullar, J.L. Gilbert, Cathodic activation and inflammatory species are critical to stimulating *in vivo* Ti-6Al-4V selective dissolution, Acta Biomater. 149 (2022) 399–409, https://doi.org/10.1016/j.actbio.2022.07.020.
[16] Y. Liu, J.L. Gilbert, The effect of simulated inflammatory conditions and fenton chemistry on the electrochemistry of CoCrMo alloy, J. Biomed. Mater. Res. B Appl. Biomater. 106 (2017) 209–220, https://doi.org/10.1002/jbm.b.33830.
[17] Y. Liu, J.L. Gilbert, Effect of simulated inflammatory conditions and potential on dissolution and surface oxide of CoCrMo alloy: in situ electrochemical atomic force microscopy study, Electrochim. Acta 262 (2018) 252–263, https://doi.org/10.1016/j.electacta.2017.12.151.
[18] M.J. Wiegand, T.Z. Benton, J.L. Gilbert, A fluorescent approach for detecting and measuring reduction reaction byproducts near cathodically-biased metallic surfaces: reactive oxygen species production and quantification, Bioelectrochemistry 129 (2019) 235–241, https://doi.org/10.1016/j.bioelechem.2019.05.020.
[19] M.J. Wiegand, G.W. Kubacki, J.L. Gilbert, Electrochemical potential zone of viability on CoCrMo surfaces is affected by cell type: macrophages under cathodic bias are more resistant to killing, J. Biomed. Mater. Res. 107 (2018) 526–534, https://doi.org/10.1002/jbm.a.36567.
[20] J.S. Pan, M.Z. Hong, J.L. Ren, Reactive oxygen species: a double-edged sword in oncogenesis, World J. Gastroenterol. 15 (2009) 1702–1707, https://doi.org/10.3748/wjg.15.1702.
[21] J. Kim, J.L. Gilbert, Cytotoxic effect of galvanically coupled magnesium-titanium particles, Acta Biomater. 30 (2016) 368–377, https://doi.org/10.1016/j.actbio.2015.11.030.
[22] G. Song, A. Atrens, D. StJohn, An hydrogen evolution method for the estimation of the corrosion rate of magnesium alloys, in: S.N. Mathaudhu, A.A. Luo, N. R. Neelameggham, E.A. Nyberg, W.H. Sillekens (Eds.), Essential Readings in Magnesium Technology, Springer, Cham, 2016, https://doi.org/10.1007/978-3-319-48099-2_90.
[23] A.L. Di Virgilio, M. Reigosa, M.F.L. de Mele, Biocompatibility of magnesium particles evaluated by in vitro cytotoxicity and genotoxicity assays, J. Biomed. Mater. Res., Part B 99B (2011) 111–119, https://doi.org/10.1002/jbm.b.31877.
[24] N.K. Nga, N.T. Thuy Chau, P.H. Viet, Preparation and characterization of a chitosan/MgO composite for the effective removal of reactive blue 19 dye from aqueous solution, J. Sci.: Adv. Mater. Devices 5 (2020) 65–72, https://doi.org/10.1016/j.jsamd.2020.01.009.
[25] A. Behnami, J.P. Croué, E. Aghayani, M. Pourakbar, A catalytic ozonation process using MgO/persulfate for degradation of cyanide in industrial wastewater: mechanistic interpretation, kinetics and by-products, RCS Adv. 11 (2021) 36965–36977, https://doi.org/10.1039/D1RA07789A.
[26] R. Gao, et al., Fabrication of superhydrophobic magnesium alloy through the oxidation of hydrogen peroxide, Colloids Surf. A Physicochem. Eng. Asp. 436 (2013) 906–911, https://doi.org/10.1016/j.colsurfa.2013.08.020.
[27] J.L. Wang, S. Mukherjee, D.R. Nisbet, N. Birbilis, X.B. Chen, *In vitro* evaluation of biodegradable magnesium alloys containing micro-alloying additions of strontium, with and without zinc, J. Mater. Chem. B 3 (2015) 8874–8883, https://doi.org/10.1039/C5TB01516B.
[28] A.M. Galow, A. Rebl, D. Koczan, S.M. Bonk, W. Baumann, J. Gimsa, Increased osteoblast viability at alkaline pH in vitro provides a new perspective on bone regeneration, Biochem. Biophys. Rep. 10 (2017) 17–25, https://doi.org/10.1016/j.bbrep.2017.02.001.
[29] L.E. Monfoulet, et al., The pH in the microenvironment of human mesenchymal stem cells is a critical factor for optimal osteogenesis in tissue-engineered constructs, Tissue Eng. 20 (2014) 1827–1840, https://doi.org/10.1089/ten.TEA.2013.0500.
[30] Y. Shen, et al., Bone regeneration: importance of local pH- strontium-doped borosilicate scaffold, J. Mater. Chem. 22 (2012) 8662–8670, https://doi.org/10.1039/C2JM16141A.
[31] W. Liu, et al., Spatial distribution of biomaterial microenvironment pH and its modulatory effect on osteoclasts at the early stage of bone defect regeneration, ACS Appl. Mater. Interfaces 11 (2019) 9557–9572, https://doi.org/10.1021/acsami.8b20580.
[32] L. Jin, Y. Nonaka, S. Miyakawa, M. Fujiwara, Y. Nakamura, Dual therapeutic action of a neutralizing anti-FGF2 aptamer in bone disease and bone cancer pain, Mol. Ther. 24 (2016) 1974–1986, https://doi.org/10.1038/mt.2016.158.
[33] J. Xu, et al., PDGFRα reporter activity identifies periosteal progenitor cells critical for bone formation and fracture repair, Bone Res 10 (2022) 7, https://doi.org/10.1038/s41413-021-00176-8.
[34] Y. Hou, et al., PDGFRA exhibits potential as an indicator of angiogenesis within the tumor microenvironment and is up-regulated in BLCA, Microvasc. Res. 151 (2024) 104614, https://doi.org/10.1016/j.mvr.2023.104614.
[35] K. Ichikawa, S.W. Miyano, Y. Minoshima, J. Matsui, Y. Funahashi, Activated FGF2 signaling pathway in tumor vasculature is essential for acquired resistance to anti-VEGF therapy, Sci. Rep. 10 (2020) 2939, https://doi.org/10.1038/s41598-020-59853-z.
[36] C. Lee, et al., VEGF-B prevents excessive angiogenesis by inhibiting FGF2/FGFR1 pathway, Signal Transduct. Targeted Ther. 8 (2023) 305, https://doi.org/10.1038/s41392-023-01539-9.
[37] J. Xu, Z. Li, Y. Hou, W. Fang, Potential mechanisms underlying the Runx2 induced osteogenesis of bone marrow mesenchymal stem cells, Am. J. Transl. Res. 7 (2015) 2527–2535. https://pmc.ncbi.nlm.nih.gov/articles/PMC4731654/.
[38] S. Vimalraj, Alkaline phosphatase: structure, expression and its function in bone mineralization, Gene 754 (2020) 144855, https://doi.org/10.1016/j.gene.2020.144855.
[39] J. Chen, et al., IL-6: the link between inflammation, immunity and breast cancer, Front. Oncol. 12 (2022) 903800, https://doi.org/10.3389/fonc.2022.903800.
[40] K. Pricola, N.Z. Kuhn, H. Haleem-Smith, Y. Song, R.S. Tuan, Interleukin-6 maintains bone marrow-derived mesenchymal stem cell stemness by an ERK1/2-dependent mechanism, J. Cell. Biochem. 108 (2009) 577–588, https://doi.org/10.1002/jcb.22289.
[41] C. Loebel, E.M. Czekanska, M. Bruderer, G. Salzmann, M. Alini, M.J. Stoddart, *In vitro* osteogenic potential of human mesenchymal stem cells is predicted by runx2/sox9 ratio, Tissue Eng. 21 (2015) 115–123, https://doi.org/10.1089/ten.tea.2014.0096.
[42] J.L. Kelts, J.J. Cali, S.J. Duellman, J. Shultz, Altered cytotoxicity of ROS-inducing compounds by sodium pyruvate in cell culture medium depends on the location of ROS generation, SpringerPlus 4 (2015) 269, https://doi.org/10.1186/s40064-015-1063-y.
[43] A. Kasatkin, A. Urakov, Effect of hydrogen peroxide on erythrocyte temperature in vitro, Chem. Biol. Interact. 354 (2022) 109837, https://doi.org/10.1016/j.cbi.2022.109837.
[44] K.M. Kim, Y.J. Lim, W.G. Jang, Policosanol stimulates osteoblast differentiation via adenosine monophosphate-activated protein kinase-mediated expression of insulin-induced genes 1 and 2, Cells 12 (2023) 1863, https://doi.org/10.3390/cells12141863.
[45] A. Suzuki, M. Minamide, C. Iwaya, K. Ogata, J. Iwata, Role of metabolism in bone development and homeostasis, Int. J. Mol. Sci. 21 (2020) 8992, https://doi.org/10.3390/ijms21238992.
[46] C. Lan, et al., miRNA-429 suppresses osteogenic differentiation of human adipose-derived mesenchymal stem cells under oxidative stress via targeting SCD-1, Exp. Ther. Med. 19 (2020) 696–702, https://doi.org/10.3892/etm.2022.11311.
[47] A. Pecci, X. Ma, A. Savoia, R.S. Adelstein, MHY9: structure, functions and role of non-muscle myosin IIA in human disease, Gene 664 (2018) 152–167, https://doi.org/10.1016/j.gene.2018.04.048.
[48] O.G. Davies, et al., Osteoblast-derived vesicle protein content is temporally regulated during osteogenesis: implications for regenerative therapies, Front. Bioeng. Biotechnol. 7 (2019) 00092, https://doi.org/10.3389/fbioe.2019.00092.
[49] Y. Chen, A. Aiken, S. Saw, A. Weiss, H. Fang, R. Khokha, TIMP loss activates metalloproteinase-tnfα-DKK1 Axis to compromise Wnt signaling and bone mass, J. Bone Miner. Res. 34 (2019) 182–194, https://doi.org/10.1002/jbmr.3585.
[50] B. Tan, X. Xu, Q. Zhang, Z. Yuan, J. Dong, The tumor suppressive role of TIMP3 in the human osteosarcoma cells, J. Orthop. Sci. 27 (2022) 689–695, https://doi.org/10.1016/j.jos.2021.02.004.
[51] F. Furlan, et al., Urokinase plasminogen activator receptor affects bone homeostasis by regulating osteoblast and osteoclast function, J. Bone Miner. Res. 22 (2007) 1387–1396, https://doi.org/10.1359/jbmr.070516.
[52] L. Hu, et al., Apoptosis repressor with caspase recruitment domain (ARC) promotes bone regeneration of bone marrow-derived mesenchymal stem cells by activating fgf-2/PI3K/akt signaling, Stem Cell Res. Ther. 12 (2021) 185, https://doi.org/10.1186/s13287-021-02253-5.
[53] D. Zhang, et al., MMP-10 deficiency effects differentiation and death of chondrocytes associated with endochondral osteogenesis in an endemic osteoarthritis, Cartilage 13 (2022) 19476035221109226, https://doi.org/10.1177/19476035221109226.
[54] C.M. Della Corte, et al., Role and targeting of anaplastic lymphoma kinase in cancer, Mol. Cancer 17 (2018) 30, https://doi.org/10.1186/s12943-018-0776-2.
[55] PIK3C2G Phosphatidylinositol-4-Phosphate 3-Kinase Catalytic Subunit Type 2 Gamma [Homo Sapiens (Human)], National Library of Medicine, 2024. https://www.ncbi.nlm.nih.gov/gene/5288. (Accessed 4 October 2024).
[56] S.H. Song, et al., Fibroblast growth factor 12 is a novel regulator of vascular smooth muscle cell plasticity and fate, Arterioscler. Thromb. Vasc. Biol. 36 (2016) 1928–1936, https://doi.org/10.1161/ATVBAHA.116.308017.
[57] Y. Yeo, et al., FGF12 (fibroblast growth factor 12) inhibits vascular smooth muscle cell remodeling in pulmonary arterial hypertension, Hypertension 76 (2020) 1778–1786, https://doi.org/10.1161/HYPERTENSIONAHA.120.15068.
[58] K. Nagasaki, A. Yamada, K. Sasa, R. Kamijo, Kielin/chordin-like protein enhances induction of osteoblast differentiation by bone morphogenetic protein-2, FEBS Open Bio 13 (2023) 1357–1364, https://doi.org/10.1002/2211-5463.13652.

[59] H.M. Cho, et al., Transplantation of hMSCs genome edited with LEF1 improves cardio-protective effects in myocardial infarction, Mol. Ther. Nucleic Acids 6 (2020) 1186–1197, https://doi.org/10.1016/j.omtn.2020.01.007.

[60] D.M. Hermann, C. Kleinschnitz, Thrombomodulin, a master switch controlling poststroke microvascular remodeling and angiogenesis, Arterioscler. Thromb. Vasc. Biol. 40 (2020) 2818–2820, https://doi.org/10.1161/ATVBAHA.120.315425.

[61] HAS 1 Hyaluronan Synthase 1 [Homo Sapiens (Human)], National Library of Medicine, 2024. https://www.ncbi.nlm.nih.gov/gene/3036. (Accessed 4 November 2024).

[62] W. Singhatanadgit, M. Varodomrujiranon, Osteogenic potency of stem cell-based genetic engineering targeting Wnt3a and Wnt9a, Cent. Eur. J. Biol. 6 (2011) 963–972, https://doi.org/10.2478/s11535-011-0079-8.

[63] L. Wang, Y.Y. Shao, R.T. Ballock, Z. Carboxypeptidase, CPZ) links thyroid hormone and Wnt signaling pathways in growth plate chondrocytes, J. Bone Miner. Res. 24 (2009) 265–273, https://doi.org/10.1359/jbmr.081014.

[64] C6 Complement C6 [Homo Sapiens (Human)], National Library of Medicine, 2024. https://www.ncbi.nlm.nih.gov/gene?Db=gene&Cmd=ShowDetailView&TermToSearch=729. (Accessed 4 November 2024).

[65] J.R. Dunkelberger, W.C. Song, Complement and its role in innate and adaptive immune responses, Cell Res. 20 (2010) 34–50, https://doi.org/10.1038/cr.2009.139.

[66] X. Liang, et al., ELMO1 regulates RANKL-stimulated differentiation and bone resorption of osteoclasts, Front. Cell Dev. Biol. 9 (2021) 702916, https://doi.org/10.3389/fcell.2021.702916.

[67] X. Yu, Z. Li, BLID: a novel tumor-suppressor gene, Oncol. Res. 22 (2015) 333–338, https://doi.org/10.3727/096504015X14410238486568.

[68] Y. Farid, N.S. Bowman, P. Lecat, Biochemistry, Hemoglobin Synthesis. In *StatPearls [Internet]*, StatPearls Publishing, Treasure Island (FL), 2024. https://www.ncbi.nlm.nih.gov/books/NBK536912/.

[69] X.D. Wang, J. Lu, Y.S. Lin, C. Gao, F. Qi, Functional role of long non-coding RNA CASC19/miR-140-5p/CEMIP Axis in colorectal cancer progression in vitro, World J. Gastroenterol. 25 (2019) 1697–1714, https://doi.org/10.3748/wjg.v25.i14.1697.

[70] S. Wang, C. Qiao, J. Li, S. Liu, P. Li, LncRNA CASC19 promotes gastric cancer progression through preventing CREB1 protein ubiquitin/proteasome-dependent degradation, Carcinogenesis 44 (2023) 209–220, https://doi.org/10.1093/carcin/bgad001.

[71] Y.J. Wu, Q.S. Yang, H. Chen, J.T. Wang, W.B. Wang, L. Zhou, Long non-coding RNA CASC19 promotes glioma progression by modulating the miR-454-3p/rab5a Axis and is associated with unfavorable MRI features, Oncol. Rep. 45 (2021) 728–737, https://doi.org/10.3892/or.2020.7876.

[72] Y. Xu, et al., KLHL38 involvement in non-small cell lung cancer progression via activation of the akt signaling pathway, Cell Death Dis. 12 (2021) 556, https://doi.org/10.1038/s41419-021-03835-0.

[73] M. Darweesh, et al., ZC3H11A loss of function enhances NF-κB signaling through defective IκBα protein expression, Front. Immunol. 13 (2022) 1002823, https://doi.org/10.3389/fimmu.2022.1002823.

[74] L. Jiang, J. Sun, D. Huang, Role of slit/robo signaling pathway in bone metabolism, Int. J. Biol. Sci. 18 (2022) 1303–1312, https://doi.org/10.7150/ijbs.66931.

[75] J. Lee, et al., ARHGEF16, A novel Elmo1 binding partner, promotes clearance of apoptotic cells via RhoG-dependent Rac1 activation, Biochim. Biophys. Acta 1843 (2014) 2438–2447, https://doi.org/10.1016/j.bbamcr.2014.07.006.

[76] K. Ishida, C. Acharya, B.A. Christiansen, J.H.N. Yik, P.E. DiCesare, D. R. Haudenschild, Cartilage oligomeric matrix protein enhances osteogenesis by directly binding and activating bone morphogenetic protein-2, Bone 55 (2013) 23–35, https://doi.org/10.1016/j.bone.2013.03.007.

[77] V. Mlakar, S.J. Mlakar, J. Zupan, R. Komadina, J. Prezelj, J. Marc, ADRA2A is involved in neuro-endocrine regulation of bone resorption, J. Cell Mol. Med. 19 (2015) 1520–1529, https://doi.org/10.1111/jcmm.12505.

[78] G. Bildik, X. Liang, M.N. Sutton, R.C. Bast Jr, Z. Lu, DIRAS3: an imprinted tumor suppressor gene that regulates RAS and PI3K-driven cancer growth, motility, autophagy, and tumor dormancy, Mol. Cancer Therapeut. 21 (2022) 25–37, https://doi.org/10.1158/1535-7163.MCT-21-0331.

[79] G. Bildik, et al., DIRAS3 induces autophagy and enhances sensitivity to anti-autophagic therapy in KRAS-driven pancreatic and ovarian carcinomas, Autophagy 20 (2024) 675–691, https://doi.org/10.1080/15548627.2023.2299516.

[80] B. Wu, et al., MRPS30-DT knockdown inhibits breast cancer progression by targeting jab1/cops5, Front. Oncol. 9 (2019) 1170, https://doi.org/10.3389/fonc.2019.01170.

[81] L. Jin, et al., SFRP2 enhances the osteogenic differentiation of apical papilla stem cells by antagonizing the canonical WNT pathway, Cell. Mol. Biol. Lett. 22 (2017) 14, https://doi.org/10.1186/s11658-017-0044-2.

[82] L. Fernandez de Castro, et al., Secreted frizzled related-protein 2 (Sfrp2) deficiency decreases adult skeletal stem cell function in mice, Bone Res. 9 (2021) 49, https://doi.org/10.1038/s41413-021-00169-7.

[83] B. Nardelli, et al., Osteostat/TNFSF18 inhibits osteoclastogenesis and is selectively expressed by vascular endothelial cells, Endocrinol 147 (2006) 70–78, 10.1210.en.2005-0518.

[84] E. Zampeli, E. Tiligada, The role of histamine H4 receptor in immune and inflammatory disorders, Br. J. Pharmacol. 157 (2009) 24–33, https://doi.org/10.1111/j.1476-5381.2009.00151.x.

[85] K.R. Martin, J.C. Barrett, Reactive oxygen species as double-edged swords in cellular processes: low-dose cell signaling versus high-dose toxicity, Hum. Exp. Toxicol. 21 (2002) 71–75, https://doi.org/10.1191/0960327102ht213oa.

[86] J. Kim, J.L. Gilbert, The effect of cell density, proximity, and time on the cytotoxicity of magnesium and galvanically coupled magnesium-titanium particles *in vitro*, J. Biomed. Mater. Res. 106 (2018) 1428–1439, https://doi.org/10.1002/jbm.a.36334.

[87] Z. Zhang, L. Yao, J. Yang, Z. Wang, G. Du, PI3K/Akt and HIF-1 signaling pathway in hypoxia-ischemia, Mol. Med. Rep. 18 (2018) 3547–3554, https://doi.org/10.3892/mmr.2018.9375.

[88] H.S. Li, et al., HIF-1α protects against oxidative stress by directly targeting mitochondria, Redox Biol. 25 (2019) 101109, https://doi.org/10.1016/j.redox.2019.101109.

[89] J. Li, et al., HIF1α-BNIP3-Mediated mitophagy protects against renal fibrosis by decreasing ROS and inhibiting activation of the NLRP3 inflammasome, Cell Death Dis. 14 (2023) 200, https://doi.org/10.1038/s41419-023-05587-5.

[90] S.H. Baek, Y.K. Jang, AMBRA1 negatively regulates the function of ALDH1B1, a cancer stem cell marker, by controlling its ubiquitination, Int. J. Mol. Sci. 22 (2021) 12079, https://doi.org/10.3390/ijms222112079.

[91] A. Vallée, Y. Lecarpentier, J.N. Vallée, The key role of the WNT/β-Catenin pathway in metabolic reprogramming in cancers under normoxic conditions, Cancers 13 (2021) 5557, https://doi.org/10.3390/cancers13215557.

[92] J.H. Lim, Y.S. Chun, J.W. Park, Hypoxia-inducible factor-1 obstructs a Wnt signaling pathway by inhibiting the hARD1-mediate activation of beta-catenin, Cancer Res. 68 (2008) 5177–5184, https://doi.org/10.1158/0008-5472.CAN-07-6234.

[93] M.D. Kuczler, A.M. Olseen, K.J. Pienta, S.R. Amend, ROS-induced cell cycle arrest as a mechanism of resistance in polyaneuploid cancer cells (PACCs), Prog. Biophys. Mol. Biol. 165 (2021) 3–7, https://doi.org/10.1016/j.pbiomolbio.2021.05.002.

[94] G. Song, Control of biodegradation of biocompatable magnesium alloys, Corrosion Sci. 49 (2007) 1696–1701, https://doi.org/10.1016/j.corsci.2007.01.001.

[95] F. Witte, The history of biodegradable magnesium implants: a review, Acta Biomater. 6 (2010) 1680–1692, https://doi.org/10.1016/j.actbio.2010.02.028.

[96] C.S. Huang, T. Kawamura, Y. Toyoda, A. Nakao, Recent advances in hydrogen research as a therapeutic medical gas, Free Radic. Res. 44 (2010) 971–982, https://doi.org/10.3109/10715762.2010.500328.

[97] R. Singh, P.P. Manna, Reactive oxygen species in cancer progression and its role in therapeutics, Explor. Med. 3 (2022) 43–57, https://doi.org/10.37349/emed.2022.00073.

[98] R.N. Goddu, et al., Chronic exposure of the RAW246.7 macrophage cell line to H2O2 leads to increased catalase expression, Free Radic. Biol. Med. 126 (2018) 67–72, https://doi.org/10.1016/j.freeradbiomed.2018.07.021.

[99] P. Wang, et al., Macrophage achieves self-protection against oxidative stress-induced ageing through the mst-nrf2 Axis, Nat. Commun. 10 (2019) 755, https://doi.org/10.1038/s41467-019-08680-6.

[100] C. López-Otín, M.A. Blasco, L. Partridge, M. Serrano, G. Kroemer, Hallmarks of aging: an expanding universe, Cell 186 (2023) 243–278, https://doi.org/10.1016/j.cell.2022.11.001.

[101] S. Staehlke, et al., ROS dependent wnt/β-catenin pathway and its regulation on defined micro-pillars-A combined in vitro and in silico study, Cells 9 (2020) 1784, https://doi.org/10.3390/cells9081784.

[102] L. Topol, W. Chen, H. Song, T.F. Day, Y. Yang, Sox9 inhibits Wnt signaling by promoting β-catenin phosphorylation in the nucleus, J. Biol. Chem. 284 (2009) 3323–3333, https://doi.org/10.1074/jbc.M808048200.

[103] T.N. Huu, et al., Redox regulation of PTEN by peroxiredoxins, Antioxidants 10 (2021) 302, https://doi.org/10.3390/antiox10020302.

[104] M.A. Chetram, et al., ROS-mediated activation of AKT induces apoptosis via pVHL in prostate cancer cells, Mol. Cell. Biochem. 376 (2013) 63–71, https://doi.org/10.1007/s11010-012-1549-7.

[105] M. Oginuma, Y. Harima, F. Xiong, O. Pourquié, Intracellular pH controls Wnt signaling downstream of glycolysis in the vertebrate embryo, bioRxiv (2018), https://doi.org/10.1101/481259.